ACS APPLIED MATERIALS & INTERFACES

www.acsami.org

Research Article

Zein-Coated Zn Metal Particles-Incorporated Nanofibers: A Potent Fibrous Platform for Loading and Release of Zn Ions for Wound Healing Application

Sita Shrestha, Bishnu Kumar Shrestha, Felix Tettey-Engmann, Reedwan Bin Zafar Auniq, Kiran Subedi, Sanjaya Ghimire, Salil Desai, and Narayan Bhattarai*

Cite This: *ACS Appl. Mater. Interfaces* 2024, 16, 49197−49217

Read Online

ACCESS | Metrics & More | Article Recommendations | Supporting Information

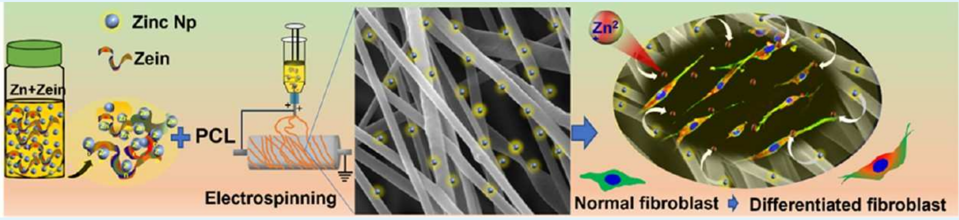

ABSTRACT: Metal particles incorporated into polymer matrices in various forms and geometries are attractive material platforms for promoting wound healing and preventing infections. However, the fate of these metal particles and their degraded products in the tissue environment are still unknown, as both can produce cytotoxic effects and promote unwanted wound reactions. In this study, we develop biodegradable fibrous biomaterials embedded with metal particles that have an immune activation functions. Initially, biodegradable zinc (Zn) nanoparticles were modified with zein (G), a protein derived from corn. The zein-coated zinc particles (Z−G) were then embedded in polycaprolactone (P) fibers at different weight ratios to create fibrous biomaterials via electrospinning, which were subsequently analyzed for potential wound healing applications. We performed multimodal evaluations of the fibrous scaffolds, examining physicochemical properties such as fiber morphology, mechanical strength, hydrophilicity, degradation, and release of zinc ions (Zn^{2+}), as well as biological properties, including in vitro cell culture studies. We provide evidence that the integration of 2.4 wt % of Z−G particles in polycaprolactone (PCL) nanofibrous scaffolds improved its physicochemical and biological functions. The in vitro cellular response of the scaffolds was evaluated using a series of cytotoxicity assays and immunocytochemistry analyses with three different cell types: mouse-derived fibroblast cell lines (NIH/3T3), human dermal fibroblasts (HDFn), and human umbilical vein endothelial cells (HUVECs). The composite fibrous scaffold exhibited robust activation and proliferation of NIH/3T3 and HDFn cells, along with a significant angiogenic potential in HUVECs. Immunocytochemistry confirmed elevated expression of vimentin and α-smooth muscle actin (α-SMA), suggesting that NIH/3T3 and Haden cells were highly differentiated into myofibroblasts. Additionally, the increased expression of CD31 and VE-cadherin in HUVECs suggests that the scaffold supports tube formation, thereby enhancing neovascularization and promoting an effective immune response. Overall, our findings demonstrate the regenerative potential of the self-enhanced Zn hemostatic bioscaffolds, which deliver both Zn^{2+} ions and zein proteins to nourish cells. This capability not only modulates cellular activities but also contributes to tissue repair and remodeling, making the scaffolds suitable for wound repair and various bioengineering applications.

KEYWORDS: *zinc, zein, electrospinning, hydrophilicity, fibroblasts, immunocytochemistry*

1. INTRODUCTION

Wound healing is a dynamic and coordinated biological process that involves hemostasis, inflammation, cell proliferation, migration, and maturation to restore cellular architecture and function.[1] The sequential growth and metabolic regulation of tissues in the wound sites promote wound healing. Usually, traumatic injuries, disruption of surgeries, and infectious diseases cause wounds. Chronic wounds are characterized by perpetuated inflammation that impairs the subsequent proliferative and remodeling phases of tissue and inhibits wound healing. Many factors, including, but not limited to, insufficient oxygen supply, lack of sufficient proteins, minerals, and vitamins influence the delaying of wound healing.[2] Biomaterials-based approaches such as polymeric films, fibers, and hydrogels incorporated with metallic particles, antibiotics,

Received: August 10, 2024
Revised: August 26, 2024
Accepted: August 26, 2024
Published: September 5, 2024

https://doi.org/10.1021/acsami.4c13458

antimicrobial drugs, and adhesive proteins have received extensive attention in repairing chronic wounds.[3] These biomaterials stimulate the deposition of the extracellular matrix and the formation of new tissues in wounds. However, there are still significant challenges in treating complicated wounds such as diabetic wounds and burns. Therefore, there is an unmet need for efficient biomaterials that can substitute or minimize the use of drugs and effectively promote tissue regeneration and wound repair. We aim to design a micronutrient-rich fibrous biomaterial highly compatible with primary endothelial cells and human dermal fibroblasts that could have promising applications in wound healing and several other biomedical applications, including tissue engineering and drug delivery.

Metallic micro- and nanoscale particles have been widely applied in the biomedical field, demonstrating therapeutic efficacy and facilitating both in vitro and in vivo clinical translation due to their ability to interact with proteins and nucleic acids.[4] In particular, the microparticles of Zn, Mg, Fe, and other metallic elements have shown enormous potential in the regulation of tissue repair and the prevention of infection.[5] These metal particles behave as biocatalysts that regulate complex biological processes related to the expression of genes, protein synthesis, and signal transduction.[6] Additionally, biodegradable metals such as Mg, Zn, and their corresponding alloys are an important class of materials for implant applications such as bone fixation devices, cardiovascular stents, and surgical pins.[7] These biometals rapidly react with water to release metal ions (i.e., Zn^{2+} and Mg^{2+}) and hydrogen. Both reaction products have clinically beneficial properties such as antioxidant properties reduction of inflammation, and the promotion of tissue repair.[8]

Zinc binding cofactors influence the cell type-specific gene expression, metabolic regulation of immunological/hemostatic transcription factors, and mRNA stability by enzymatic saturation.[9] The presence of zinc cofactor mediates human umbilical vein endothelial cells (HUVECs) to express kininogen, responsible for the activation of human plasma and intrinsic clotting pathway, modulation of inflammation severity, and regulation of cell proliferation.[10] Noteworthy, Zn particles promote the dermal cell types to neutralize the excessive production of reactive oxygen species (ROS) in the metabolic process and inhibit bacterial infection. Zn^{2+} and Mg^{2+} released from a hydrogel enhance the deposition of extracellular matrix (ECM) in cells and tissues.[11] These ions stimulate human skin fibroblasts (HFSs) to differentiate into myofibroblasts and immortalized keratinocyte functions by the activation of STAT3 signaling and promote wound repair. The Mg^{2+} also activates the upregulation of Zn^{2+} ions in HSFs, enabling their therapeutic efficiency for wound remodeling and healing processes. Note that, the concentration of zinc (≥ 50 μM) in the cell medium activates the ILC2 cells with increased intracellular Zn level and elevates the expression of the type 2 cytokines (IL5, IL2RA, and IL1RL1).[12] These cytokines are responsible for the immune response, macrophage activation, and protection against bacterial and parasitic invasions in the body. Additionally, zinc at micromolar levels binds with cysteine residues to protect the cytoskeleton network of vimentin filaments, ensuring cellular architecture, signaling, and epithelial-mesenchymal transitions in human fibroblasts. The uptake of zinc through vimentin-zinc interactions induces vimentin polymerization and enhances the wound healing process.[13] Prior studies showed that the controlled release of Zn ions (0.035 mM after 3 days) from polycaprolactone (PCL)-chitosan fibrous scaffold significantly increased NIH/3T3 growth and proliferation, indicating that the zinc-chitosan complex is prominent and biologically active.[14] Aside from the promising benefits of Zn particles in tissue engineering, physical immobilization of these particles into cell-instructive scaffolds presents multiple challenges. These challenges include issues with dispersibility and solubility, as well as oxidation of the particles during multistep postsynthetic procedures, which increases their reactivity and charges. Consequently, excessive free zinc efflux from scaffold materials might create zinc accumulation around living cells leading to toxic effects.[15] Therefore, we first developed coated Zn particles with zein to prevent rapid oxidation of Zn and embedded those particles in polymeric nanofibers via electrospinning. Numerous functional groups of zein such as nitrogen-based through glutamine residues are capable of forming zinc-zein linkages via a polar loop of amino acids. This can form an adsorbed “corona” around the bare Zn particles, forming Z−G particles. Additionally, zein is known for its antioxidant and antibacterial capacity and has been found to enhance the growth of human dermal fibroblasts and skin-wound healing process.[16] The composite nanofibrous scaffolds can control the degradation of Zn in complex biological environments.

Here, we report on Z−G particles incorporated into PCL nanofiber scaffolds, which act as self-nourishing structures that significantly promote fibroblast proliferation and differentiation as well as induce endothelial cells for vascularization and tissue regeneration. Our novel surface coating technique with zein is cost-effective and eco-friendly. We characterized the coated Zn particles and assessed their impact on the physical, chemical, and mechanical properties of the scaffolds. Subsequently, we studied cellular responses in vitro using fibroblast cells (both mouse and human) and endothelial cells (HUVECs). We hypothesized that the combined effects of Zn as a micronutrient, zein as an antioxidant protein, and PCL nanofibers as a physical support would collectively enhance biological functionality to promote cell growth and development. This promising biomaterial scaffold aims to overcome the limitations of pristine nanoparticles and accelerate cellular functions around the wound, advancing wound care and tissue regeneration applications.

2. EXPERIMENTAL SECTION

2.1. Materials and Reagents. Polycaprolactone (PCL, M_W = 80,000), zein (G), and zinc nanoparticles (Zn NPs) were purchased from Sigma-Aldrich. Trifluoroethanol (TFE, purity ∼99+%), Dulbecco’s modified Eagle’s medium (DMEM), fetal bovine serum (FBS), penicillin/streptomycin (P/S), AlamarBlue, and 3-(4,5-dimethyl-2-thazolyl)-2,5-diphenyl-2*H*-tetrazolium bromide (MTT, methylthiazoyldiphenyl-tetrazolium bromide) assay kits were purchased from Thermo Fisher Scientific (Waltham, MA). All chemicals and reagents were of analytical grade and used as received without any further purification.

2.2. Preparation of Zein-Coated Zinc Particles. Zein solution was prepared by dispersing zein powder (2% w/w) in TFE, followed by continuous stirring for 12 h at room temperature (RT). Then, 4.0 g of Zn NPs was added into the as-prepared zein solution in TFE to make a total weight of 75.0 g of a colloidal solution (stock solution) of Z−G particles. The mixture was probe sonicated (Model: FB 120, S/N 60663T-11−10, Fischer Scientific) for 8 h with a 30:10 pulse rate in an ice bath. Conjugation of zein with the Zn surface led to the formation of Z−G particles through the solvation effect.[17] The well-dispersed Z−G colloidal solution was used to fabricate nanofibrous

Table 1. Sample Designation and Composition

materials	PCL-P (g)	zein-G (g)	calculated composition		composition obtained from ICP-OES analysis	
			zinc-Z (g)	P:Z:G (w/w) %	zinc-Z (g)	P:Z:G (w/w) %
PZ0G0	1.5			100:0:0		100:0:0
PZ0G2	1.5	0.3		83.4:0:16.6		83.4:0:16.6
PZ1G2	1.5	0.3	0.025	82.2:1.4:16.4	0.02	82.3:1.2:16.5
PZ2G2	1.5	0.3	0.050	81.1:2.7:16.2	0.04	81.3:2.4:16.3

scaffolds after characterizing the microstructure, crystallinity, and chemical compositions of the particles.

2.3. Fabrication of Nanofibrous Scaffolds. Electrospinning was used for the fabrication of nanofibrous scaffolds. The scaffolds were fabricated with different weight percentages of Z−G particles (prepared in Section 2.2) with PCL. Different volumes of Z−G colloidal (e.g., 0.5, 1, and 2 mL) from the stock solution were blended with PCL/zein solution. The weight ratio of PCL/zein was maintained as ∼83/17 (w/w %). The solution of PCL in TFE with zein was first prepared under magnetic stirring for 8 h before the addition of Z−G colloidal particles. Each homogeneous mixture of PCL/zein/Z−G particles was further subjected to magnetic stirring overnight and was loaded in a syringe for electrospinning. All of the parameters for the electrospinning procedure were fixed according to our previous publication.[14] Table 1 shows the composition of fabricated scaffolds. For a comparative study, PCL-zein fibrous scaffolds without Zn particles were also fabricated. First, zein solution was prepared in TFE at three different percentages (i.e., 1, 2, and 3 wt %). Then, 10 wt % PCL was blended with each zein solution in an airtight vessel using a magnetic stirrer overnight and used for electrospinning. All of the resulting fibrous meshes were dried at 40 °C overnight before further analysis and characterization. The amount of PCL-P, Zein-G, and Zinc-Z were expressed in gram (g). Proportions of each component in the dry samples were calculated both empirically, by comparing the weights of material used initially, and experimentally, by analyzing the scaffold materials with inductively coupled plasma (ICP)-OES analysis.

3. CHARACTERIZATION OF SCAFFOLDS

3.1. Physicochemical Characterization. Scanning electron microscopy (SEM, Jeol-800) equipped with energy-dispersive X-ray spectroscopy (EDS) (Quantax 70, Bruker Corporation, Billerica, MA) was used to observe the morphology of the Zn and Z−G particles and the surface morphology of the fibrous scaffolds. For the SEM imaging, the Zn and Z−G particles were well dispersed in pure ethanol separately, and then 5 μL of each colloidal solution was dropped on aluminum foil. The solvent was completely evaporated. For the surface morphology of fibrous scaffolds, the samples were prepared by cutting into small pieces, attaching them to carbon tape, and sputter-coating with gold-palladium using a coating device (Leica EM ACE200, IL) for 30 s (coating depth = 5 nm) at 15 mA. SEM images were taken at an accelerating voltage of 3 kV. The morphologies of the particles were further observed by high-resolution transmission electron microscopy (HRTEM; JEM-2100Plus-JEM). X-ray photoelectron spectroscopy (XPS) analysis was performed using a TSCALAB XI+ X-ray Photoelectron Spectrometer (Thermo Scientific Escalab Xi+ XPS). The hydrodynamic diameter of nonspherical Zn and Z−G nanoparticles was measured by Malvern Zetasizer (ZEN3600; Malvern Instruments, Inc. Westborough, MA). The crystallinity of each material was also examined using X-ray diffraction (XRD, Rigaku Japan) with a Cu target at a wavelength (λ) of 0.154 nm with a 2θ range of (10−90)° at a scan rate of 5°/min. The Fourier transmission infrared (FTIR) spectra of the samples were recorded by an FTIR spectrometer (Agilent 670, Sant Clara, CA). The melting and crystallinity of the electrospun samples were evaluated using a Mettler Toledo DSC3+ equipped with a differential scanning calorimetry (DSC) sensor with 56/120 thermocouples. Nanofibrous specimens of approximately 5 mg were sealed in an aluminum pan with an empty pan as a reference. Afterward, samples were subjected to heating−cooling cycles from 25 to 120 °C at a rate of 10 °C min^{-1}. All DSC measurements were conducted under a high-purity nitrogen atmosphere at a flow rate of 10 mL/min. The crystallinity of the samples was calculated using the relation $X_c = \frac{\Delta H_m}{\Delta H_0} \times 100\%$, where X_c is the degree of crystallinity, ΔH_m is the enthalpy of melting for the samples, and ΔH_0 is the theoretical melting enthalpy of PCL (100% crystalline) which was taken as 135 J/g. The mechanical property of the different fibrous scaffolds (card template, each of area; 60 × 40 mm^2) was examined by using a microsystems tensile testing machine (TA. XT plus C texture Analyzer, Texture Technologies Corp, South Hamilton, MA). The concentrations of zinc were quantified utilizing the Optima 8300 inductively coupled plasma-optical emission spectrometry (ICP-OES), PerkinElmer, Inc. For ICP analysis, samples underwent digestion employing the MARS 6 microwave digester, produced by CEM Technologies, Inc.

3.2. Wetting and Swelling Property. The wettability of the fibrous scaffolds was determined through the static contact angle measurement using the sessile drop method (KRUSS drop shape analyzer, DSA25E, Germany) at RT. The optical image of each electrospun scaffold absorbing water droplets was taken at two different time points (10 and 30 s) after the deposition of droplets on the surface of the scaffolds (n = 5). Further, the swelling behavior of scaffolds was evaluated as previously reported in the literature.[18] Briefly, each scaffold of dimension (20 × 20 mm^2) as a test specimen was measured for the initial dry weight (W_d). Then, the scaffolds were carefully placed in a 10 mL phosphate buffer solution (PBS 1×) with pH 7.4 at 37 °C in an incubator separately. After a specific time interval, nanofibrous scaffolds were removed and washed several times with water then held over tissue paper (absorbent paper) amidst gentle tapping to remove adsorb PBS on the surface. Each wet sample was identified as a swollen scaffold (n = 3) and weight was represented as (W_s). The gravimetric method was applied to calculate the swelling ratio expressed in percent (%) using the relation $(S_w) = \frac{W_s - W_d}{W_d \times 100}(\%)$.

3.3. Protein Adsorption Analysis. Adsorption of protein on the fibrous scaffolds was evaluated using a bicinchoninic acid assay kit (Pierce BCA Protein Assay Kit; Thermo Scientific) according to the manufacturer's instructions. The BSA as a standard solution (pH 7.2) was used to calculate the total protein absorbed on the scaffolds. Each scaffold (n = 3) was immersed in a cell growth medium incubated at 37 °C for 24 h. Then, the medium was aspirated followed by washing

https://doi.org/10.1021/acsami.4c13458
ACS Appl. Mater. Interfaces 2024, 16, 49197−49217

with PBS 3 times before adding the BCA reagent to the scaffold and incubated for 30 min at 37 °C. A similar process was employed for each of the scaffold ($n = 3$) cultured with NIH/3T3 cells for 24 h for comparison. After the incubation time was completed, the absorbance was recorded at 570 nm using a microplate reader (CLARIOstar Plus, BMG Labtech, Inc., Cary, NC).

3.4. In Vitro Release of Zn Ions and Degradation of Fibrous Scaffolds. The release of Zn^{2+} ions from the scaffolds was analyzed to confirm the cytotoxicity evaluation in vitro. Each scaffold ($n = 3$) of diameter 12 mm was prepared on glass coverslips and fixed at the bottom of 48-well plates. The scaffolds were sterilized and washed with 1× PBS. Then, NIH/3T3 cells were cultured onto the scaffolds (see details of cell culture in Section 3.5). At each time interval (for example; 1, 3, 5, 7, 9, and 12 days) the cell media was collected and the release of Zn^{2+} ion concentration was examined for each time using an inductively coupled plasma emission spectroscope (IPC-OES Optima 8300. PerkinElmer, Shelton, Connecticut) according to our prior publication.[14] Further, the degradation of the scaffolds was analyzed under SEM. Briefly, the scaffolds were immersed in the cell-cultured medium for 30 days with refreshing the cultured media every 3 days. Finally, the scaffolds were washed with deionized water several times and dried before SEM observation.

3.5. Cell Culture Study. Mouse fibroblast cell line (NIH/3T3) (ATCC Cell Line Bank 1658, Manassas, VA) were cultured with DMEM supplemented with 10% FBS and 1% P/S, in a 37 °C incubator with 5% carbon dioxide (CO_2) and 95% humidified atmosphere. Primary Dermal Fibroblast Normal; Human Neonatal (HDFn, ATCC cell bank) were cultured in Fibroblast Basal Medium (ATCC PCS-201−030) with Fibroblast Growth Kit-Serum Free (ATCC PCS-201−040) containing each of the following growth supplements: L-glutamine, hydrocortisone hemisuccinate, HLL supplement (Human serum albumin, linoleic acid, lecithin), rh FGF β, rh EGF/TGF β−1 supplement, rh insulin, and ascorbic acid long with Streptomycin-Amphotericin B Solution (ATCC PCS-999−002; dilution 1:1000) in a 37 °C incubator with 5% CO_2 and 95% humidified atmosphere. Human Umbilical Vein Endothelial Cells (HUVECs) (ATCC CRL-1730) were cultured in F-12K Medium (ATCC 30−2004) and Heparin solution (Sigma, H3393) supplemented with 10% FBS (ATCC 30−2020) and Endothelial cell growth supplement (ECGS; Fisher Scientific, CB-40006) in a 37 °C incubator in 5% CO_2 and 95% air atmosphere. The fresh cell culture medium was replenished every second day of the culture period for all of the cell types. After 80% confluency, the cells were passaged by dissociation with trypsin-EDTA (Gibco, Thermo Fisher Scientific).

3.6. Biocompatibility and Cell Proliferation Study. The prepared scaffolds were fitted on circular glass coverslips (12 mm diameter) and fixed at the bottom of 48-well plates (Thermo Fisher). Prior to cell seeding, the prepared samples were sterilized under ultraviolet (UV) light for 3 h and washed with 70% ethanol, followed by PBS (1×). The cells were seeded at a density of 1.5×10^4/well, pipetting at the center of scaffolds after pretreating the samples soaking in the medium for 1 h. The cells were nourished with a fresh culture medium every 2 days. The biocompatibility of the scaffolds and proliferation of the cells on the scaffolds were examined using AlamarBlue (AB) colorimetric assay according to the company's protocol. The absorbance of the AB was measured at 570 nm using 600 nm as a reference wavelength by a microplate reader (Varioskan LUX, SN 3020−81747, Theromoscientific spectrophotometer, Singapore). Furthermore, the proliferation and survivability of the NIH/3T3 cells and HDFn on each scaffold were evaluated using an MTT assay kit under the company's protocol. For the MTT test, the seeding of cells was performed similar to that of cells cultured in AB condition as described above and the optical density (OD) was recorded at 540 nm.

In addition, the cytotoxicity of the scaffolds was determined with a live/dead assay kit (PerkinElmer LLC Via AOPI Staining Solution; Fisher Scientific). The NIH/3T3 cells and HDFn were cultured on various scaffolds as described above for 5 days. Live cells were stained with green and red for dead cells. Cells were visualized under an Olympus I × 83 microscope incorporated with Olympus cell Sens Dimension (Olympus Corporation, Shinjuku, Tokyo, Japan). Further, live and dead cells were counted on each scaffold ($n = 3$) from the fluorescence images using ImageJ software (J 1.53c, NIH, Bethesda, MD).

3.7. Cell Attachment and Morphology Study. The morphology, growth, and proliferation of viable NIH/3T3 and HDFn cells on the scaffolds were observed under a fluorescence microscope after 1 and 5 days of culture at 37 °C. The cells were seeded on different scaffolds similar to the prior method and cultured up to day in 48-well plates. The cells were washed with PBS (1×) and fixed with 4% paraformaldehyde (PFA, Thermo Scientific) solution for 10 min. The fixed cells were permeabilized in 0.3% Triton X-100 (Thermo Scientific) for 3 min at RT. Then, the cells were blocked with 1% BSA for 30 min at RT. Subsequently, the cells were stained with ActinGreen 488 Readyprobes reagent (Invitrogen, Thermo Fisher Scientific) for cytoplasm about 20 min, and DAPI (4′6,-diamidino-2-phenylindole, Dihydrochloride; Invitrogen, Thermo Fisher Scientific), for nuclei until 5 min at RT in the dark condition. The fluorescence images were taken using an Olympus I × 83 microscope (Olympus). Further, the NIH/3T3 cells and HDFn attachment on different scaffolds were also observed using SEM. Cells on the scaffolds were first rinsed with PBS and then fixed with 2.5% glutaraldehyde solution and dehydrated with 30, 50, 70, and 90% ethanol serially. All scaffolds were dried in a hood for 1 day at RT before SEM observation.

3.8. Immunocytochemistry (ICC) Analysis. The heterogeneity of the NIH/3T3 fibroblast and differentiation study of HDFn was identified using the immunocytochemistry technique as per Abcam protocol. Briefly, the cultured NIH/3T3 cells and HDFn were washed with PBS and fixed with 4% paraformaldehyde (PFA). The fixed cell samples were permeabilized with 0.2% Triton X-100 for 5 min at RT. Using PBS-T, samples were rinsed and blocked the nonspecific binding sites with 1% BSA for 30 min. Sequentially, the cells were incubated with primary antibodies anti-vimentin (ab8978, abcam) and anti-alpha smooth muscle actin (ab124964, abcam) at 4 °C overnight. Subsequently, after washing with PBS-T, the cells were labeled again with secondary antibodies, including goat antirabbit IgG H&L (Alexa Fluor 488; ab150077, abcam) and goat antimouse IgG H&L (Alexa Fluor 594; ab150116, abcam) for 1 h at RT under dark condition. The nuclei were counter-stained with DAPI for 10 min. Then, the Olympus I × 83 microscope (Olympus) was used to visualize fluorescence images of stained cells. The fluorescence intensity of the cytoplasmic protein markers

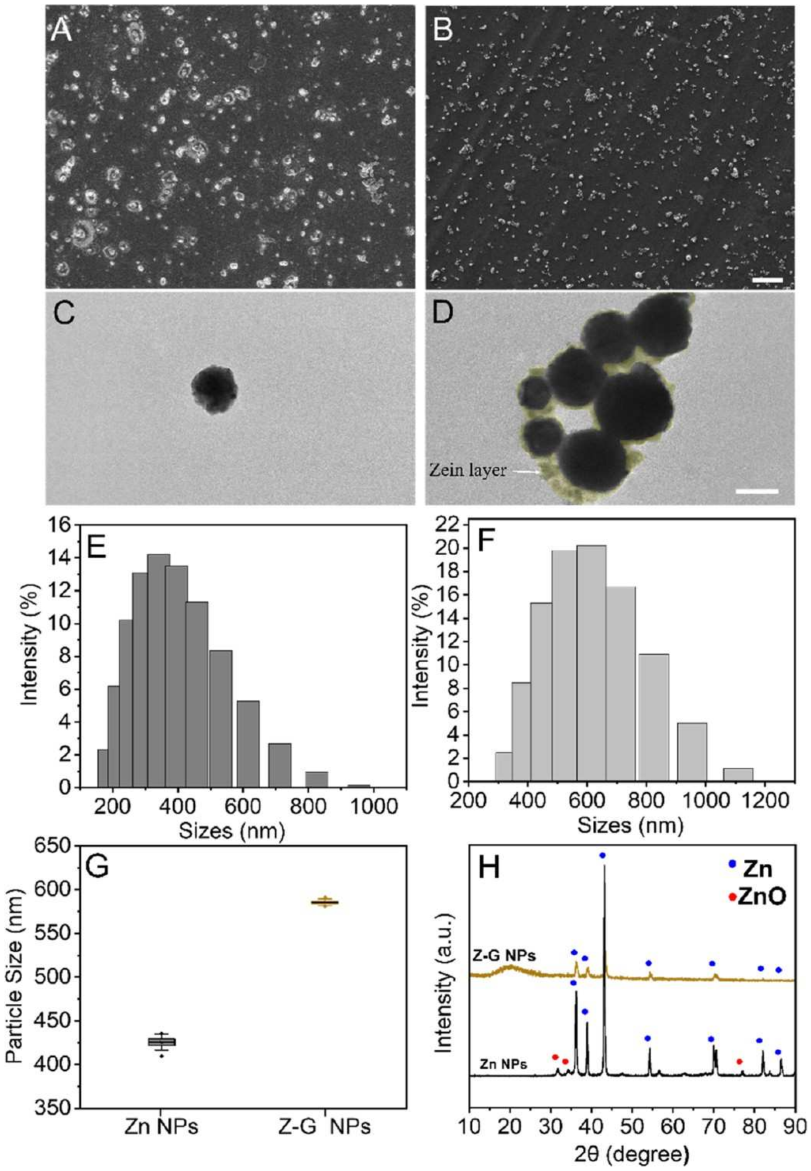

Figure 1. Characterization of Zn NPs and zein-coated Zn particles. (A, B) SEM images of received Zn metal particles and zein-coated Z−G particles, respectively (scale bar = 10 μm). (C, D) Representative TEM images of pure Zn NPs and Z−G NPs, respectively (scale bar = 100 nm). (E, F) Hydrodynamic size distribution of Zn NPs and Z−G NPs expressed in intensity percentage measured by DLS analysis. (G) Average particle sizes measured by DLS analysis. (H) XRD patterns of the Zn NPs with and without zein coating.

(vimentin and α-SMA) were expressed after analyzed by the ImageJ software.

3.9. In Vitro Study of Angiogenic Activity and Tube Formation. The angiogenic properties of HUVECs were conducted by cell migration and a tube formation assay. The cell migration capability of HUVECs that represent a wound healing scenario was assessed via an in vitro scratch assay. Briefly, HUVECs were seeded at a density of 1.5 × 10^5/well in 24-well plates. At 80% confluency, the cells were wounded by scraping with a 200 μL pipet tip, denuding a strip of the monolayer. Then, the cells were washed with PBS and incubated with cell culture media eluted (extracts) from scaffolds (PZ0G0, PZ0G2, PZ1G2, and PZ2G2) for 24 h, while the freshly prepared media was used as control. The variation in the wound diameter was determined and normalized in three different experiments. The wound area was observed and photographed using a phase contrast inverted microscope at 0 and 24 h. Then, the percentage of the cell-free area due to cell migration was measured and quantified using a wound healing assay tool from ImageJ Software.

To determine the effect of the scaffolds on the angiogenic properties, a tube formation assay was conducted with the HUVEC cells. Briefly, 24-well plates were coated with ice-cold Matrigel Matrix Basement Membrane (ref- 354234, Corning) and incubated at 37 °C for at least 1 h to allow solidification. HUVECs were then harvested from the culture plate and seeded at a density of 1.5 × 10^5 cells per well onto the Matrigel layer, followed by incubation at 37 °C. After 3 and 6 h of incubation, images of the tubular structures were captured using an inverted microscope. Quantification of the data was performed using the Angiogenesis Analyzer in ImageJ Software.

3.10. Immunocytochemistry (ICC) Analysis of HUVECs. For immunostaining of vascular endothelial VE-cadherin and the endothelial cell marker CD31, HUVECs

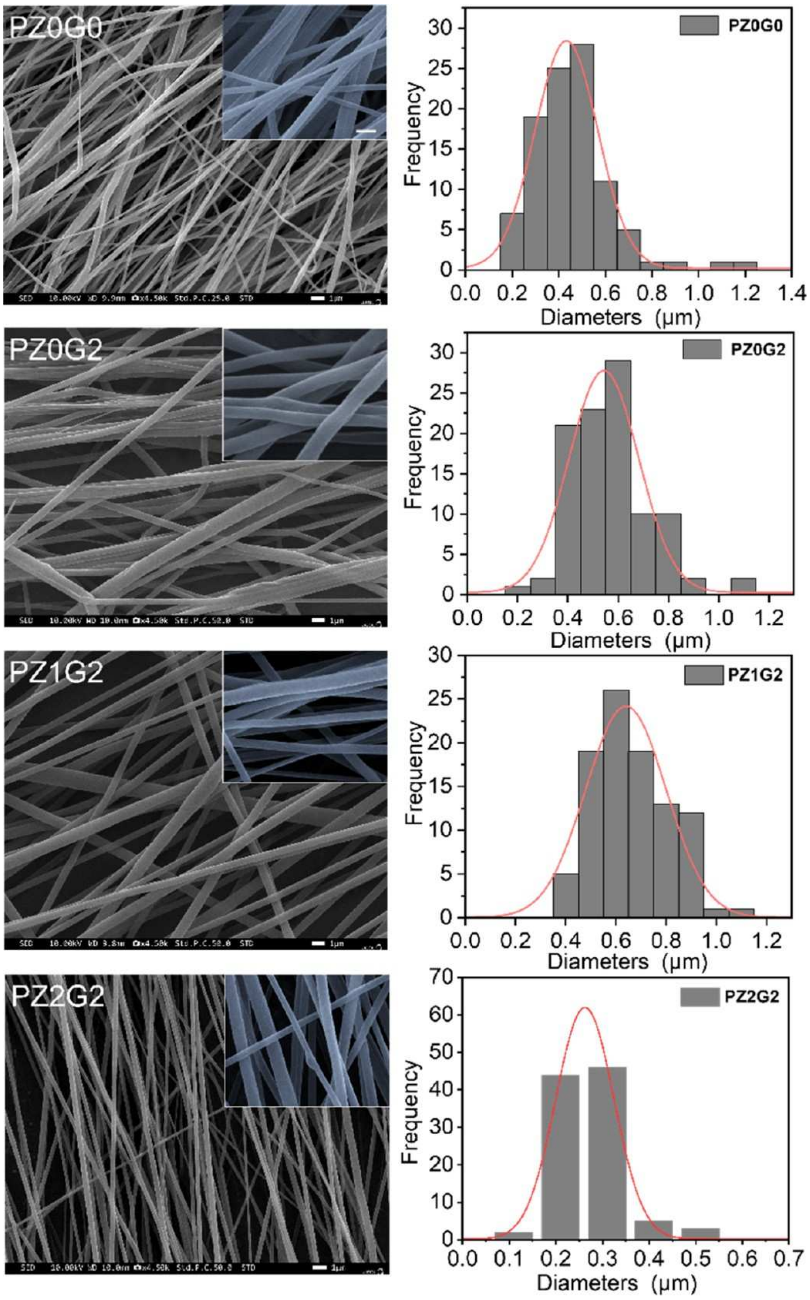

Figure 2. Surface morphology and diameter distributions of the electrospun fibrous scaffolds. SEM micrographs at the left column and insets show the morphology of the fibers at different compositions. Scale bars = 500 nm for all insets. The frequency distribution curves expressed in histograms on the right column correspond to the diameters of the nanofibers ($n = 100$) obtained from SEM images on the left column. The diameter was measured using ImageJ software.

were seeded in 48-well plates and cultured for 7 days in extracted culture media from different samples, as well as in freshly prepared media for the control cells. Subsequently, cells were fixed with 4% PFA followed by washing with PBS. Then, permeabilized with Triton X-100 and blocked the nonspecific proteins with 2% BSA. Sequentially, the cells were incubated with primary antibodies; anti-VE-cadherin Polyclonal Antibody (PA5−19612, Thermo Fisher Scientific, Invitrogen) and anti-CD31 antibody (ab24590, abcam) for 1h at RT, followed by a further incubation at RT for 1h with secondary antibodies; goat antirabbit IgG H&L (Alexa Fluor 488; ab150077, abcam) and goat antimouse IgG H&L (Alexa Fluor 594; ab150116, abcam). F-actin was labeled with ActinGreen 488 ReadyProbes Reagents (Alexa Fluor 488 phalloidin) and ActinRed 555 ReadyProbes Reagent (Rhodamine phalloidin). DAPI was used to label nuclear DNA in blue. Stained cells were imagined using a fluorescence microscope (Olympus I × 83 microscope).

3.11. Statistical Analysis. Data were plotted using OriginPro software version 2023 (Origin Lab, Northampton, MA). Microsoft Excel was used to analyze all quantitative data and presented as the mean ± standard deviation (SD, $n = 3$). A one-way analysis of variance (ANOVA) testing followed by Tukey's post hoc analysis was used to determine the statistically significant differences between groups and significance was considered at p values of $^{*}p < 0.05$, $^{**}p < 0.01$, and $^{***}p < 0.001$.

4. RESULTS AND DISCUSSION

4.1. Characterization of Zein-Coated Zn Particle. Nanoscale-sized Zn particles with a wide range in diameter were successfully obtained using an ultraprobe sonication technique. SEM and TEM micrographs (Figure 1) confirm that these particles are dispersed but susceptible to aggregate in any media. However, most particles are relatively smaller in size, similar to the commercial scale as received. High-resolution Zn particles show a relatively hexagonal or spherical structure assigned to the structure of zinc nanoplate.[19] The SEM images of Z−G NPs exhibited a well-dispersed colloidal form. Notably, the TEM image shows a thin layer of zein protein on the surface of the Zn NPs, suggesting that a nanoscale protein layer is formed. The layer with variable thickness was observed due to the ultrasonic treatment during coating. The zein has the ability to cap Zn NPs strongly due to the high electron density in zein and the oxidative property of Zn. It is well known that certain amino groups in zein, such as glutamine and alanine act as ligands (chelating agents) forming molecular linkage to nanoparticles through coordinate bonds named biofunctionalization that enhance particles' physicochemical stability and increase bioactivity.[20] The surface modification of the particles by protein exhibits amphipathic properties, which also improves biodistribution in any media through polar functional groups. The sizes of the particles were further evaluated by the dynamic light scattering (DLS) analysis (Figure 1E,F). The Zn NPs show a wide range in sizes (100−800 nm), which was found to be ∼60% by quantitative measurement with respect to intensity. In contrast, the size of Z−G colloidal was measured from 300 to 1100 nm, where ∼65% of the particles were in the range of 300−600 nm sizes. Overall, the average size (425.7 ± 8.7 nm) of Zn NPs and (585.4 ± 3.6 nm) of Z−G particles were measured (Figure 1G). The larger size may be the result of particle agglomeration. However, these average values are not consistent compared to the actual size (90−250 nm) of the particles observed by TEM. The characteristic diffraction peaks (Figure 1H) at 2θ = 31.7, 36.3, 39.01, 54.2, and 70.1° are assigned to (002), (100), (101), (102), and (110) planes of Zn, respectively, and are indexed to metallic Zn (ICCD File no. 00−004−0831). Instead, some other low-intensity peaks were observed due to the oxidation of zinc into ZnO. It may have occurred during a short-time exposure to air. Notably, all of the peaks corresponding to zinc oxide were absent in the Z−G complex particles, suggesting that the Zn NPs were completely protected from oxidation.

The zein-coated Zn particles were analyzed by FTIR and XPS analysis, and the results were presented in Supporting Information (Figure S1). The FTIR absorbance peak intensity assigned to amine groups of zein were decreased in coated particles compared to the peak intensity of pure zein. This suggests that the zinc was covered with a thin layer of zein protein via bonding with the −N/O-terminal of either glutamic acid or proline components of the zein. The ratio of the peak intensity of amide II to amide I is observed greater in the Z−G particles compared to pure zein indicating that the Zn NPs have an interference effect with amide I.[21] The bonding between zein and Zn was further confirmed by XPS by analyzing the XPS survey spectra and binding energies of the −N−C and −N−H bondings. The positions of peaks corresponding to Zn $2p_{1/2}$ and Zn $2p_{3/2}$ are consistent with the results published in the previous study.[22] The binding energies of N−C and N−H were slightly changed after coating. Consequently, a slight decrease in binding energy was measured in the Zn−zein complex, indicating a possible link of Zn with nitrogen via Zn−N bodings. The spectrum of O 1s of zein shows deconvoluted peaks at 532.17 and 530.33 eV, which are assigned to C═O and $C-O^-$, respectively. The broad peak appeared at 534.16 eV confirming the bonding of metallic particles with oxygen in C−O groups of zein.[23] Thus, FTIR and XPS analyses confirm that the protein was bonded and coated on the surface of the particles through the conjugation and solvation process.

4.2. Surface Morphology of Nanofibrous Meshes. The surface morphology of the fibrous scaffolds and fiber diameter distribution curves are shown in Figure 2. The SEM images of the PZ0G0 nanofibrous scaffold show that the fibers are nonuniform with an interwoven network. The majority of fibers are in the range of 300−500 nm measured by the frequency of diameter distribution. However, the PZ0G2 scaffold shows smooth surfaced fibers and more aligned structures with fiber diameter distribution (400−600 nm). The fibers are slightly larger in diameter than PZ0G0 because of the increase in viscosity upon the addition of zein. In contrast, the consecutive increment of zein percentage, from 1 to 3 wt %, while blending with PCL interfered with the fabrication process. The composite matrix with 3 wt % zein did not produce regular fibers because of the high viscosity. Zein exhibits a reinforcement effect via interfacial nonpolar/polar covalent interactions with PCL increasing the viscosity of the blend solution. Notably, no substantial difference in diameter and morphologies of the fibers were observed with 1 wt % (image has not shown) and 2 wt % zein in fibers. Thus, 2 wt % zein was an optimized amount for preparing PZ0G2 fibers.

The addition of Z−G particles (1.2 wt %) in optimized PZ0G2 solution produces relatively uniform and continuous fibers of PZ1G2. The diameter distribution of most nanofibers was measured in the range from 400 to 600 nm. However, the diameter of fibers was measured relatively smaller while being expressed in frequency distribution as compared to PZ0G2 fibers. The presence of metallic particles increases the conductivity of the solution, as a result, the majority/higher frequency of small diameters fibers was produced.[24] PZ2G2 shows an aligned morphology and is smaller in diameter. In the inset image of PZ2G2, small beads were observed due to the presence of Z−G particles (2.4 wt %) encapsulated in fibers. The diameters of most fibers are in the range of 200 to 300 nm. Importantly, the addition of Z−G particles did not alter the morphology of the fibers remarkably suggesting that the particles were uniformly embedded and distributed within the fibers (Figure S2). However, the blending of 2 mL of Z−G colloidal with PCL/zein solution frequently blocked, clotted, and broke the fibers during electrospinning. The possible reason for the interference of fiber production might be the high viscosity, stiffness, and surface tension of the solution. The protein-rich fibrous matrix is highly advantageous in cell activities such as tissue differentiation and regeneration.[25] The Z−G particles could be a source of protein-micronutrients that can modulate cell metabolism, cell adhesion, cytoskeleton organization, phenotype, and cell differentiation.

4.3. Chemical Compositions and Degree of Crystallinity. FTIR spectra of the nanofibrous mesh and zein are shown in Figure 3A,B. Pure PCL shows major bands at 2872

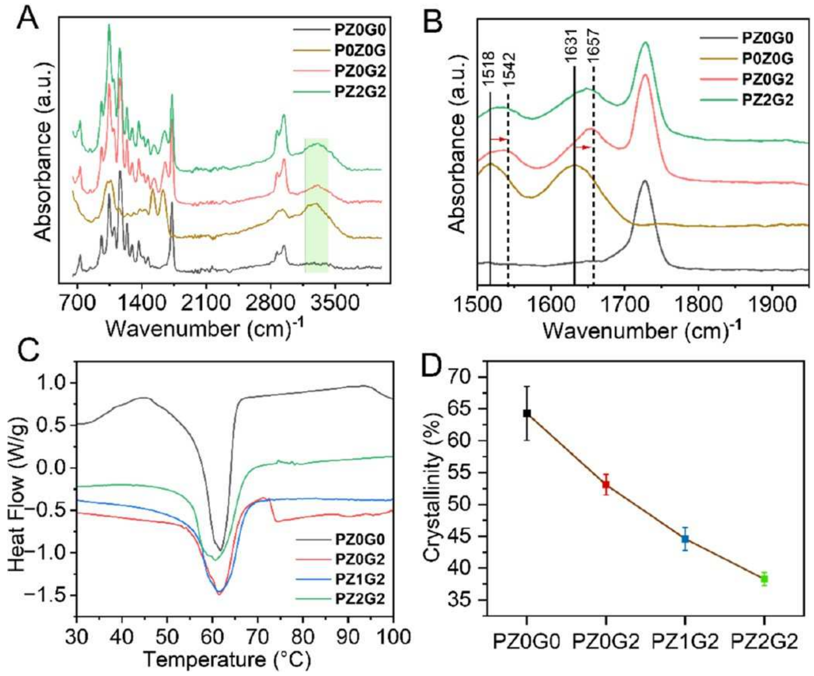

Figure 3. Analysis of chemical structures and thermal behavior of the nanofibers. (A, B) Transmission-FTIR spectra of the electrospun scaffolds. P0Z0G represents the FTIR spectrum of pure Zein. (C) DSC curves showing melting transitions of the samples with different compositions and (D) degree of crystallinity of each of the nanofibers.

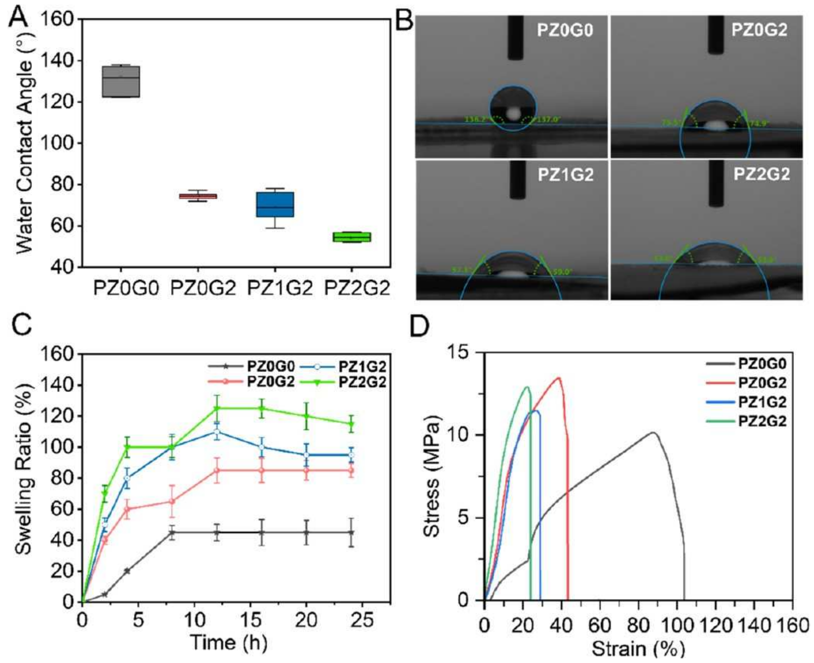

Figure 4. Analysis of surface wetting behavior and mechanical properties of various nanofibrous meshes. (A) Average water contact angles (WCA) (*n* = 5), (B) optical images of WCA after 5 s of contact time, (C) swelling behavior of the samples after immersed in water at various times, and (D) representative tensile stress−strain curves of the fibrous materials.

cm^{-1} (symmetric CH_2 stretching), 2948 cm^{-1} (asymmetric CH_2 stretching), 1727 cm^{-1} (C═O stretching), 1239 cm^{-1} (asymmetric C−O−C stretching), and 1167 cm^{-1} (C−C stretching vibration). With the addition of zein and zein-coated Zn particles to PCL, the adjacent peak position corresponding to zein relatively shifted its amide groups from 1631 to 1657 cm^{-1} (amide I) and from 1518 to 1542 cm^{-1} (amide II). These shifts of frequencies toward higher wavenumber (blue shift/increasing frequency) reveal that some of the chemical moieties of zein were involved in chemical interactions between Z−G and PCL−G. The amide and carboxylic groups of zein can interact with PCL via some interactions such as dipole−dipole interaction, hydrogen bonding, nonpolar covalent bonding, etc. In addition, such blue shifts also indicate the interaction of −COOH (carboxylic group) with the CH_2 linkage of PCL through anomalous H-bonding.[25] In such interactions, zein can lose some of its OH and NH_2 groups to form the zein−Zn and zein−PCL complexes. It also confirms that the broad peaks at 2890 and 3280 cm^{-1} are assigned to N−H (primary amide) and O−H (carboxylic group of glutamic acid), respectively, in zein. Notably, zein exhibits a promising electron donor that influences the metallic Zn to form a transient coordination complex through the glutamate (O-donor) or alanine (N-donor) groups of the zein.[26] It has been suggested that the difference in zeta potential between zinc and zein also facilitates the formation of strong bonds, where Zn is more susceptible to forming coordination complexes.[27]

Figure 3C shows the DSC curves of PCL and its blends with various Z−G contents. The semicrystallinity of PCL was confirmed by the exotherm curves at 45 °C. In addition, the endothermic peak at 61.7 °C reveals the melting temperature (T_m) of PCL.[28] Compared with pure PCL, a broad peak with slightly increased T_m was observed for all of the composite samples. This peak could be due to the possible transition between solid and liquid crystal states where a high amount of heat can only melt the polymer−protein complex. The change in molecular weight of the materials via cross-links of Z−G and PCL varies the viscoelastic properties that influence the T_m of the materials.[29] Meanwhile, the disappearance of the exothermic peak of PCL confirms the formation of the polymeric complex, which also indicates the loss of the crystalline behavior of PCL. It can be illustrated further after studying the decrease in crystallinity percentage of PCL as depicted in Figure 3D using the DSC curve. The increment in wt % of Z−G particles in composite tends to increase the destruction of regular alignments of PCL polymeric chains. This could be due to the crowding effect, the branch of Z−G linkers, and intermolecular hydrogen bonding that tends to collapse the polymer from its equilibrium state.[30] Moreover, the presence of zein-coated Zn particles embedded in the PCL acts as a plasticizer that successfully disrupts the crystallinity. Indeed, PZ0G0 with 64% of crystallinity gradually decreased to 38% in PZ2G2. It is well known that the decrease is accompanied by a decrease in the crystalline percentage and the impurities present in the fresh polymeric materials.

4.4. Wettability, Swelling Behavior, and Mechanical Properties. To evaluate the water absorption behavior of the nanofibers, we measured the static water contact angle (WCA) of the fibrous meshes. The WCA of PZ0G0, PZ0G2, PZ1G2, and PZ2G2 ($n = 5$) were found to be 131.7, 74.4, 68.8, and 54.4°, respectively (Figure 4A). The optical images referring to the WCA of the scaffolds show the surface water contact angle (WCA) and illustrate the change in surface chemistry of the scaffolds (Figure 4B). As discussed above, the lowering of WCA confirms the increase in the number of hydrogen bonds. The ample H-bonding exhibits the driving force of water, including both Laplace force and gravity that increase the capillary action of the contact surface, as a result, the water molecules are gradually percolated through the surface.[31] In addition, zein itself has amphiphilic properties with high charge density that can produce polar/nonpolar interactions. Such properties in the materials are beneficial for cell interaction, the transport of micronutrients, and protein activities in the cellular microenvironment.[32] The intrinsic hydrophobic surface is well defined in PZ0G0. In contrast, the integration of zein and Z−G particles into the biomaterials showed interesting hydrophilic properties. The presence of Z−G with the source of polar moieties enhances the surface charge density and porosity, which may ascertain the properties of high-water adsorption ability.

The swelling behavior of the nanofiber was studied based on the weight-swelling ratio at different time intervals in PBS (Figure 4C). Despite the hydrophobic behavior of PCL, the swelling results of PZ0G0 absorbed water and the degree of swelling came around 45% after immersion for 8 h and remained unchanged up to 25 h of immersion. It could be the presence of an ionic concentration gradient at the interface of PBS and PCL fibers, where the osmotic pressure was able to diffuse ions through the porous membranes, while the swelling proportion was unchanged beyond 8 h indicating the existence of dynamic equilibrium. Correspondingly, the swelling degree linearly increased over 100% after 4 h in PZ2G2 scaffolds with a higher percentage of Z−G particles, while PZ0G2 and PZ1G2 showed around 60 to 80%. A significant level of increase in the absorption ability of the materials is probably due to a number of reasons such as the hydrophilicity, highly interconnected porous structure, and large surface area. The Z−G particles accelerate the solution-material interactions that raise the intermolecular attraction force on polymeric networks. Indeed, the absorption of solution gradually stretches the polymeric chain along with buckling, wrinkling, delamination, and bending of polymeric nanofibers to increase the surface area further.[33] Subsequently, the adsorption of the ionic solution remained steady and a swelling ratio was obtained above 90 to 120% at 24 h suggesting Zn−G particles facilitate cross-linking properties to enhance swelling behavior of the materials.

The tensile mechanical properties of various fibrous meshes were performed with a load cell of 500 N and with a displacement rate of 3.5 mm/min. Results are expressed in stress vs strain curves (Figure 4D), and ultimate tensile strength, Young's modulus, and breaking strain (Table 2). The mechanical property of the scaffolds has a pivotal role in modulating the cell functions that are responsible for the growth and regeneration of tissues. The PZ0G0 scaffolds showed lower tensile strength and Young's modulus than the PZ0G2, PZ1G2, and PZ2G2. The homogeneous distribution of Z−G particles in the fibers increased tensile strength and Young modulus which decreased the breaking strain. Importantly, chemical groups in zein and Z−G particles easily form a number of interatomic and intermolecular bonds through H-bonds and polar or nonpolar bonds. Additionally, such enhanced mechanical properties could also be due to the formation of uniform and smaller fiber diameters with more aligned fibers at higher concentrations of Z−G particles. In contrast, the higher amount of Zn particles in the polymeric blends also possesses a stiffening effect (i.e., toughness and rigidity) that causes a lowering in elongation at the breakpoint. Such mechanical properties of the fibrous meshes ensure

Table 2. Mechanical Properties of the Electrospun Composite Materials

sample	ultimate tensile strength (MPa)	Young's modulus (MPa)	breaking strain (%)
PZ0G0	9.41 ± 1.04	29.77 ± 3.39	84.71 ± 8.45
PZ0G2	13.89 ± 2.11	58.52 ± 2.61	42.02 ± 3.13
PZ1G2	11.85 ± 2.58	61.74 ± 2.17	29.19 ± 1.88
PZ2G2	12.97 ± 3.31	65.55 ± 4.37	24.22 ± 3.27

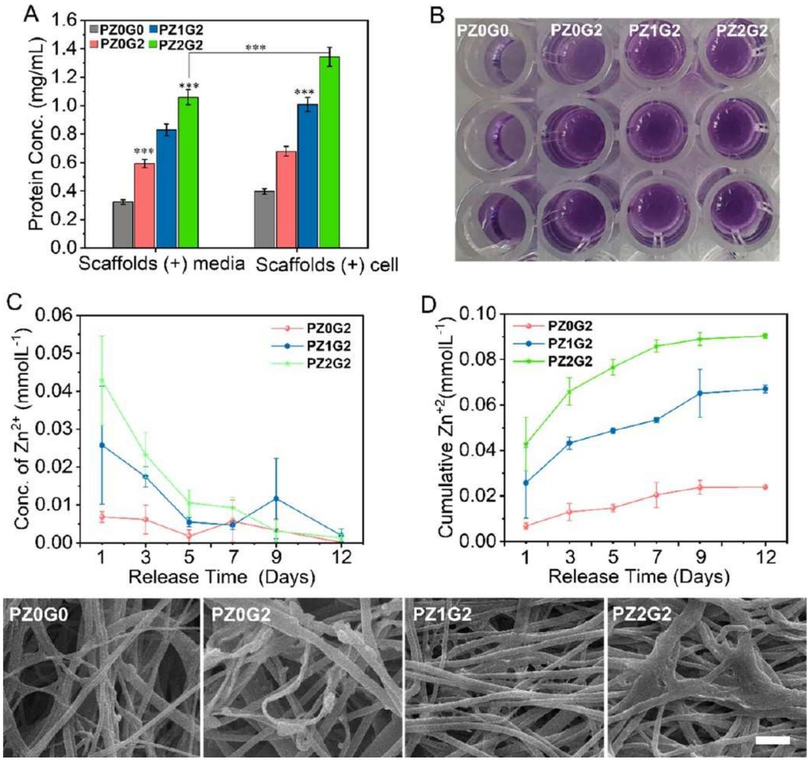

Figure 5. Analysis of protein absorption and Zn ion release behavior of the fibrous mesh scaffold under in vitro cell culture conditions. (A) Quantitative analysis of protein adsorption ability of the scaffolds in cell media with or without cell attachments for 24 h. Statistical analysis was performed using the one-way ANOVA with Tukey's post hoc method, and the data are expressed as the mean ± SD; $n = 3$ per group (where $*p < 0.05$ and $***p < 0.001$). (B) Optical images of the eluted solution from different scaffolds after being treated with BCA protein assay kits and (C, D) representative release profiles of Zn ions from the scaffolds cultured with NIH/3T3 cells at different periods ($n = 3$). SEM images (bottom row) showing the morphology of the fibers after 30 days of incubation in cell culture media. Scale bar = 2 μm.

suitable biomaterials to support cells while repairing wound defect sites.

4.5. Protein Adsorption, In Vitro Release Profile of Zn Ions, and Degradation Study.

Figure 5A,B shows the protein adsorption ability of the scaffolds. PZ0G2, PZ1G2, and PZ2G2 showed significantly higher ($P < 0.001$) concentrations of protein adsorption compared to PZ0G0. The adsorption of protein on scaffolds makes the surface more bioactive which influences the cell-materials interactions, transport of ECM and fluids around the scaffolds, and additional cellular activity including growth, proliferation, and differentiation. The adsorption mainly occurs through noncovalent bonds that arise from the side chain of protein at the interface.[34] The adsorption was found to be 3-fold higher in PZ2G2 than PZ0G0, suggesting that the proteinaceous scaffolds further encounter with active site of protein through protein−protein interaction that enhances the adsorption rate. However, the adsorption of the protein on PZ0G0 is suggested via hydrophobic interaction. In addition, we further analyzed the protein adsorption ability of the scaffolds under cell-scaffold conditions. It was found that all of the scaffolds adsorbed the protein but a significantly higher concentration ($P < 0.001$) was measured with PZ2G2 scaffolds. A high concentration of protein reveals the presence of protein molecules from cell media and protein-based ECM that are released from cells during proliferation and cell metabolism. In addition, nonpolar groups and hydrophobic domains of zein increase the ability to absorb/bind more proteins on the surface.[35] The highest adsorption capacity of PZ2G2 could be explained due to the presence of higher active surface areas, surface charge density, dipolar characteristics of PCL, and protonation of zein protein as indicated by blue shift, $-NH^{3+}$.[36,37] Furthermore, the optical micrographs confirm the higher binding affinity of the protein with PZ2G2, where Zn ions bind the protein more strongly compared with other divalent metal ions. The gradual increases in the deep violet color of the scaffolds from PZ0G0 to PZ2G2 after being treated with BCA indicates the strong interactions of the protein with the scaffolds, where the protein-Cu^{2+} complex completely reduced to Cu^{1+}. Such high protein adsorption ability of PZ2G2 might enhance the biological functions of the scaffolds such as enzymatic activity, electron transport, oxygen transport, inflammatory response, etc.[38]

Furthermore, the biodegradability of the scaffolds was examined by quantifying the amount of Zn^{2+} release and changes in the surface morphology of the scaffolds in cell culture conditions (Figure 5C,D). As expected, a high amount of Zn in PZ2G2 was released, and more Zn^{2+} was accumulated with prolonged treatment with cell media over the time of 12 days. The fibrous scaffolds soaked into cell media swelled immediately and released zinc atomic state into an ionic state. The amount of Zn ions was different at different times i.e., 7.71 ± 2.1 ppm at day 1 and 0.23 ± 0.1 ppm at 12 days. The release profile followed a linear pattern illustrating the controlled release of the Zn^{2+} from the scaffolds, indicating the degradation of scaffolds. Similar trends were observed in other scaffolds. However, Zn ions from PZ1G2 were found to be 4.2 ± 2 ppm at 1 day and followed a decrease in linear trend but a peculiar amount was released at 9 days. This could be the unexpected bursting/swelling of fibers.[39] Meanwhile, the release of Zn^{2+} from PZ0G2 was also observed in a negligible

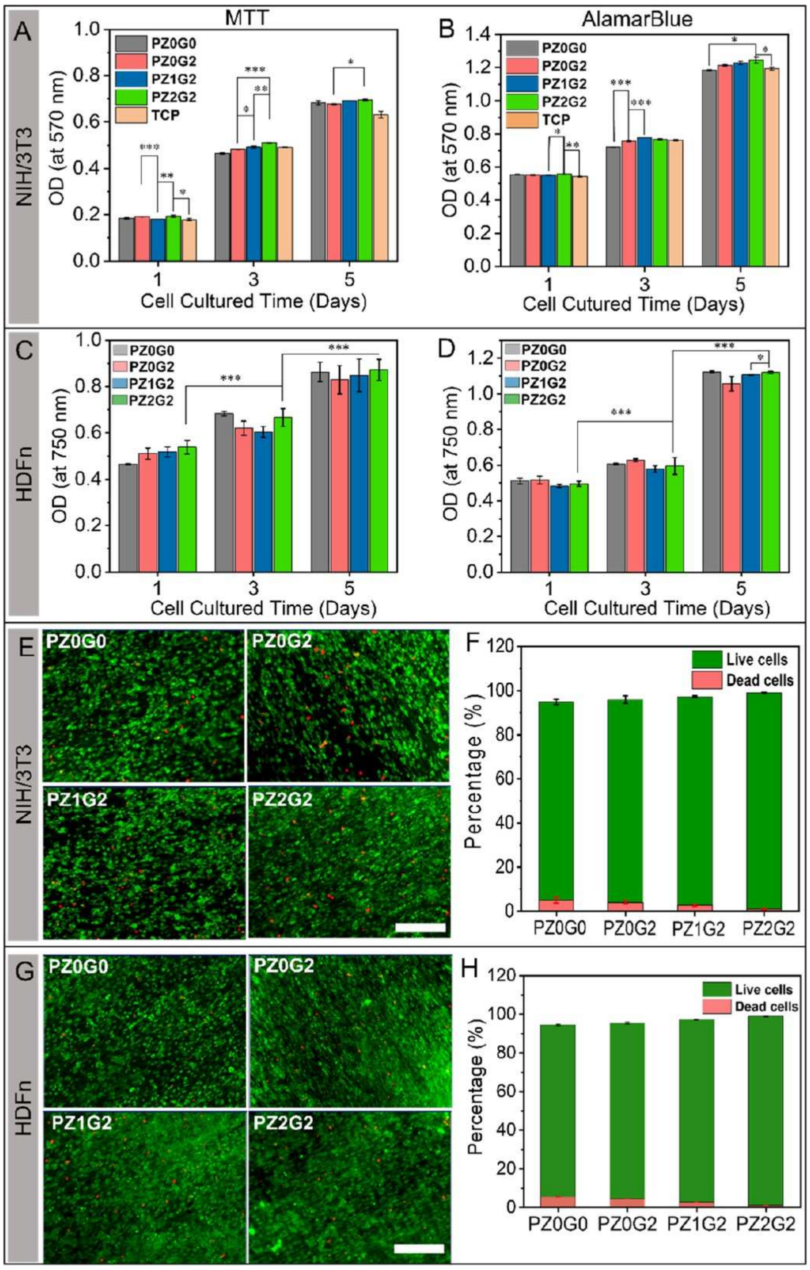

Figure 6. In vitro performance of the fibrous scaffolds for cell survivability and proliferation. In vitro study of NIH/3T3 cells and HDFn cultured on different scaffolds. (A, C) Evaluation of the metabolic activity of NIH/3T3 and HDFn cells via MTT assay. (B, D) Evaluation of cell viability of the scaffolds at days 1, 3, and 5 via AlamarBlue assay. Cell seeded on the tissue culture plate (TCP) was used as the control. (E, G) Fluorescence microscopy images of cells stained with live/dead staining dye at day 5 of the culture. Live cells (green color) and dead cells (red color) are stained using PerkinElmer LLC via acridine orange/propidium iodide (AOPI) staining solution. Scale bar = 200 μm. (F, H) The percentage of live and dead cells obtained from respective images of live and dead cells using ImageJ software. Statistical analysis was performed using the one-way ANOVA with Tukey's post hoc method, and the data are expressed as the mean ± SD; $n = 3$ per group for cell viability test (where $^{*}p < 0.05$, $^{**}p < 0.01$, and $^{***}p < 0.001$).

amount. It can be possible that the source of a minute amount of Zn is associated with the presence of Zn in serum that is often supplemented with cell media. In tissue engineering or wound healing, the cellular and extracellular interactions on the scaffold surface can be tailored by controlled degradation that regulates the release system of medication and drugs to maintain the physiological functions of the cells. It has been reported that zinc sulfate as source of zinc micronutrient (200 mg) for day one improves wound healing and tissue repair. However, above 200 mg causes serious threats such as impaired immune function, epigastric abdominal pain, vomiting, and diarrhea.[40] The cumulative value of Zn ions released is in the range of the recommended dose, suggesting that our material could be the source of Zn micronutrients to enhance wound healing and tissue regeneration. Moreover, the SEM images confirm the in vitro degradation (bottom row of Figure 5) of the scaffolds. The morphology of fibers was different from its original phase. The fibers seem deformed, discontinuous, and swollen in diameter. A notable change in surface morphology was observed in PZ2G2 scaffolds. Obviously, enzymatic activity in scaffold-cell media interaction

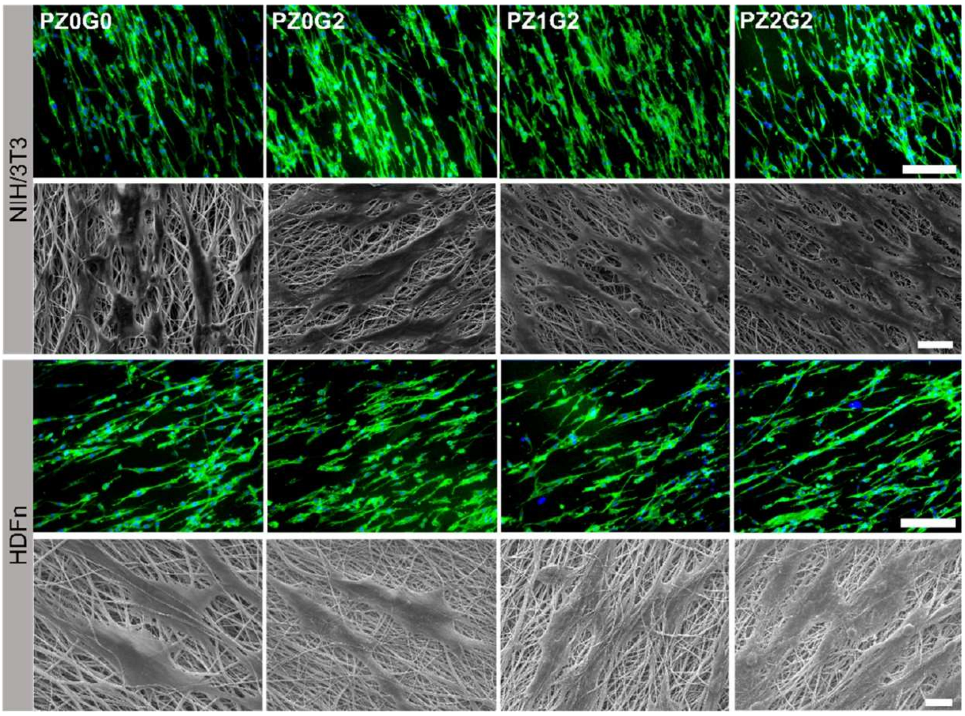

Figure 7. In vitro performance of the fibrous scaffolds and effects on the cell attachment and morphology. Fluorescence microscopy images (top rows) and SEM images (bottom rows) of NIH/3T3 cells and HDFn cultured on different fibrous scaffolds for day 5. The cytoskeleton was stained with ActinGreenTM 488 (green), and the nuclei were counter-stained with DAPI (blue). Scale bar = 200 μm. SEM images showing attachment of NIH/3T3 and HDFn fibroblasts at a magnification of 1.0k, scale bar = 20 μm (NIH/3T3), and at a magnification of 1.5k, scale bar = 10 μm (HDFn).

led to facilitating the degradation process which helps to provide a suitable platform to regenerate cells.

4.6. In Vitro Cytocompatibility and Cell Proliferation Study.

The in vitro cytocompatibility of the different scaffolds was studied with NIH/3T3 and HDFn using MTT, the AlamarBlue assay, and live and dead cell staining assay (Figure 6). To accomplish this, the cytocompatibility was assessed by analyzing the survivability, growth, and proliferation of the cells. All of the scaffold samples promoted higher cell proliferation of NIH/3T3 and HDFn cells with increased incubation times indicating good biocompatibility of the scaffolds. MTT assay evaluation of NIH/3T3 confirms that the cell proliferation rate on PZ0G2, PZ1G2, and PZ2G2 was boosted up to 2.5-fold at day 3 to 3.5-fold at day 5, respectively, compared to day 1. Similarly, the proliferation of HDFn was increased by 1.3- and 1.75-fold corresponding to days 3 and 5, respectively. Importantly, cell proliferation was significantly higher with PZ2G2 compared with PZ0G0, PZ1G2, and tissue culture surface (TCP). The optical images shown in Figure S3 illustrate the cell metabolic activity of NIH/3T3 on different scaffolds. The color change after the reduction of MTT compounds initiated by oxidoreductase enzyme secreted by cells reflects the viability and proliferation of cells on different scaffolds. The acceleration of cell growth triggers enzymatic activities, which was confirmed by observing the purple color. Our experiments proved that the dense purple color corresponds to higher enzymatic activities that occurred during cell metabolism, while a higher number of cells influence the biocatalytic activity and vice versa. Indeed, the cells on the PZ2G2 illuminated a darker purple color than others, suggesting that the cells were more activated and proliferated. As seen in AlamarBlue assay results, the PZ2G2 cell-laden scaffolds showed a high cell proliferation rate at all times. The cell viability analyses confirmed that the cell proliferation on the fibrous scaffold with a high composition of Zn−G particles (i.e., PZ2G2) differed considerably compared to the fibrous scaffold without Zn−G particles (i.e., PZ0G0) and TCP at 5 days. These results are consistent with the MTT analysis.

The incorporation of Z−G particles into the scaffolds may increase the extracellular Zn-bound protein content in the medium, enhancing the growth of NIH/3T3 and HDFn. Zn-regulated cofactors in mouse (e.g., ZNG1) and human (e.g., ZNG1E) methionine aminopeptidase 1 (METAP1) proteome contribute to protein stability, maturation, subcellular localization, and enzymatic activity.[41] Zinc-based chelating groups are known for their strong affinity to increase β-cells selectivity with replication-promoting activity by ∼250% in rats and ∼130% in humans without toxicity, suggesting that zinc-chelators are well tolerable with therapeutic relevance.[42] The Zn homeostasis in β-cells is maintained by the zinc transporter, where almost 70% of zinc from the cell is located in insulin that works for glucose metabolism.[43] Importantly, the dysfunction of β-cells triggers the destabilization of insulin, resulting in diabetes, the chronic disease responsible for the impairment of wound healing. Fibroblasts are active target cells that play crucial roles in wound healing and tissue repair. The proliferation and growth of the fibroblasts are clues that confirm the deposition of ECM, a structural framework in the vicinity of the wounds. The continued activation of fibroblasts with the PZ2G2 scaffold indicates the regenerative potential of these scaffolds, which can produce native ECM and could impact the tissue remodeling at wound healing. Furthermore, zinc-metalloproteins maintain the metal-induced oxidative

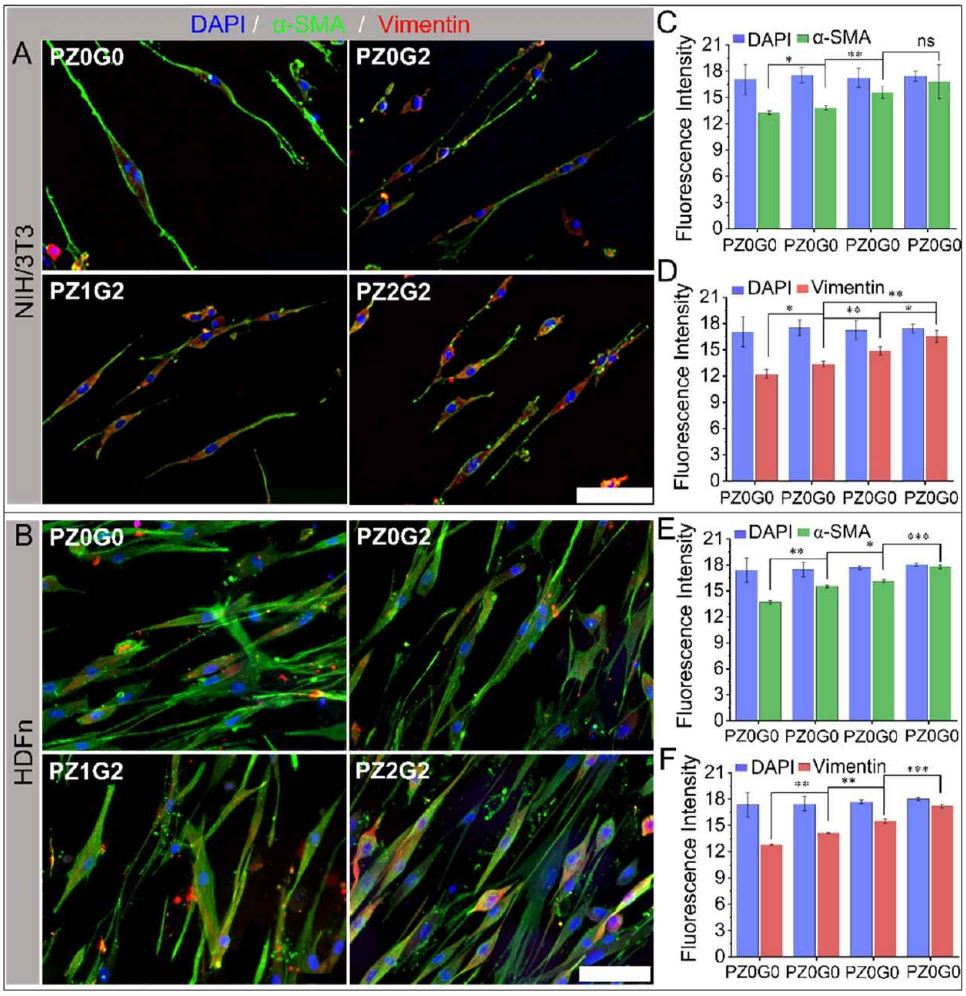

Figure 8. Immunocytochemistry of the fibroblasts showing their differentiation and heterogeneity on different scaffolds. Immunofluorescence microscopy images showing the expression of vimentins (stained red), an endogenous cytoskeleton filamentous protein, and α (α)-smooth muscle actin (green), a marker of activated myofibroblasts at day 14. (A) NIH/3T3 cells and (B) HDFn. Nuclei were counter-stained with DAPI (blue). Scale bar = 100 μm. (C, D) Quantification of the expression of DAPI, Vimentin, and α-SMA of images (A). (E, F) Quantification of the expression of DAPI, Vimentin, and α-SMA of images (B). The intensities were measured from the expression of the proteins in immunofluorescence images by the ImageJ software. Statistical analysis was performed using the one-way ANOVA with Tukey's post hoc method, and the data are expressed as the mean ± SD; $n = 3$ per group (where $^{*}p < 0.05$, $^{**}p < 0.01$, and $^{***}p < 0.001$).

damage as a scavenging oxidant by balancing cell redox activity.[44] As a proof of concept, we combined Z−G, where zein might work as a chelator moiety to extend the Zn dose up to ~2.4 wt % to promote fibroblast regeneration as compared to the previous report.[14] Meanwhile, the PLGA/β-TCP/Zn scaffold with 2 wt % of Zn also has been reported cytotoxicity to BMSCs despite its controlled release of not more than 2.055 ± 0.223 μg/mL at 16 weeks.[45] In contrast, the release of Zn^{2+} from PZ2G2 could keep the metallic ions at the required concentration to induce regeneration of fibroblasts for regeneration. It could be possible to increase the Zn content in the scaffolds as the binding capacity of zein as Z−G complex. The bioadhesive nature of zein protein exhibits the protein−protein interaction, ECM regulation, and Zn hemostasis. Notably, the high proliferation tendencies of the fibroblasts on the PZ2G2 scaffold indicate their potential bioactive platform for cell engraftment as wound-repairing scaffolds. The controlled release of Zn eliminates the zinc accumulation that could speed up or regulate the Zn uptake by cells allowing anti-inflammatory and immune-responsive properties. Our results reveal unique feature enriching Z−G micronutrient pools in the scaffolds considerably accelerating the cell fate of fibroblast for a prolonged time.

Live/dead cell fluorescence images (Figures 6(E,G) and S4) confirm the spreading and proliferation of cells on the Z−G-based scaffolds with increased cell numbers. Quantitative data show that cells seeded on PZ1G2 and PZ2G2 exhibited a high percentage of cellular viability (>97%) at day 5 (Figure 6F,H). However, the viability percentage was <95% on scaffolds without zinc during the same period. It has been known that the presence of zinc as a supplement regulates calcium homeostasis and reduces cell apoptosis.[44] These results suggest that the presence of zein in the scaffolds stabilizes the fast reactivity of Zn, preventing cell apoptosis due to high-dose Zn ions.

4.7. Cell Attachment and Morphology. The cellular mass and cell proliferation on the scaffolds gradually increased in the order of PZ0G0 < PZ0G2 < PZ1G2 < PZ2G2 as evidenced by fluorescence microscopy images in Figure 7. At day 5 of the culture, both the cytoskeleton and nuclei are highly stained and expressed in PZ2G2 samples compared to those in other sample groups, as shown in Figure 7 (top rows for both cell types). The detailed morphology of the cells is presented in Figures S5(A,B) and S6(A,B). Fibroblast cells exhibited stellate morphologies and elongated narrow dendritic-like projections. The cells were observed to migrate directionally, aligning with the microstructure of the scaffolds. Interestingly, within just one day, the cells rapidly transformed their morphologies, suggesting that the scaffolds provide a strong biomimetic surface to coordinate cell growth, proliferation, and regeneration. Notably, normal and healthy polygonal-shaped cells were extensively spread throughout the scaffold surfaces, exhibiting extensive outgrowth of pseudopodia. The Z−G incorporated scaffold surface activated the fluorescent protein in the cells, enabling the expression of ActinGreen 488, which functions as cytoskeleton staining. This indicates that the Z−G particles enhance the biocompatibility of the materials. However, the massive intra- and extracellular Zn ions could trigger mitochondrial dysfunction and damage lysosomal membranes, leading to cell apoptosis.[46] In contrast, zinc binding proteins, such as ZnMet, inhibit the generation of reactive oxygen species (ROS) and protect cells from the accumulation of ROS, thereby maintaining cellular homeostasis.[47]

Further, the adherent nature of the cells and their spindle-like morphology on the fibrous scaffolds were observed in SEM images (Figure 7). Both NIH/3T3 and HDFn fibroblasts exhibited wide cellular membranes bridging the fibers with flattened morphological structures. These cells uniformly extended their filopodia and adhered tightly to the surface, revealing that the nanoscale surface features support cell growth. The morphology of the cells seeded on PZ0G0 was observed to be spindle-shaped with a lower cell density, differing from the cells on PZ1G2 and PZ2G2 surfaces. This difference might be due to the hydrophobic nature of PCL, which provides fewer cell recognition sites. As expected, a greater number of cellular masses with polarized morphology connected by elongated dendrites were observed in the PZ1G2 and PZ2G2 scaffolds compared to those in the PZ0G0 and PZ0G2 scaffolds on day 5. The cells on these scaffolds were polygonal, well grown, and large, extending in all directions and covering almost 90% of the scaffold areas. The highly widespread cells were interconnected, suggesting the strong cytocompatibility of the scaffolds. The micronutrient-rich scaffolds might be involved in transmitting signals via ECM receptors to boost the cellular metabolism. Notably, the combination of Z−G maintains a controlled release of zinc, where an excess of Zn could participate in a hydrolytic reaction to maintain physiological conditions and activate fibroblasts and immune cells.[48] Notably, the immune cells have a high concentration of Zn level (i.e. 10−29 mM) in insulin, which encourages cells for proliferation, matrix deposition, and immune response.[49] The Zn wt % in the PZ2G2 scaffold may limit the therapeutic range that insists on the inherent immunogenicity of the cells developed on the scaffold for its validation in wound healing treatment. The release of Zn^{2+} from the scaffolds could maintain a dynamic equilibrium between intracellular and extracellular Zn ions homeostasis through transmembrane Zn transporter proteins.[50] The large and healthy fibroblast cells with increased cell proliferation, infiltration, and attachments provide evidence of scaffolds providing ECM-mimicking structures to induce tissue functions. These results indicate that Z−G particles in the fibers regulate the NIH/3T3 cell function and could be beneficial for in vivo studies. Additionally, HDFn studies serve as a powerful complement to preclinical research and may play a crucial role in wound healing studies.

4.8. Differentiation of NIH/3T3 Fibroblasts and HDFn.

To identify the heterogeneity of the fibroblasts, we performed immunocytochemistry on NIH/3T3 and HDFn cells cultured with various scaffolds. As shown in Figures 8A,B and S7, the immunofluorescence microscopy images reveal the expression of cytoplasmic proteins, including vimentin, an endogenous cytoskeletal filamentous protein, and α-SMA, a marker of activated myofibroblasts. The expression of these proteins indicates the transformation of fibroblasts into myofibroblasts as well as the differentiation of NIH/3T3 and HDFn cells. Importantly, cytoplasmic intermediates such as vimentin, microfilaments, and microtubules play key roles in cell migration, morphogenesis, and stress-bearing ability in cells interacting with surrounding tissues and substrates.[51] Especially, the expression of vimentin notifies the growth of a mature cell type and cell differentiated stages. On both days 6 (Figure S8A) and 14, the immunofluorescence images of the fibroblasts on different scaffolds illustrate a dynamic network of filamentous proteins with an increased level of expression. Indeed, the expression of both proteins was high in PZ2G2 compared with other scaffold groups in both types of fibroblasts on 14 days. Particularly, vimentin exhibits a robust filamentous framework that extends uninterrupted from the nuclear periphery to the membrane boundary. This extensive filamentous assembly in the cytoskeleton protects structural deformations and facilitates cytoskeleton cross-talk throughout the cytoplasm. Additionally, the protein is organized in an extended fibrillar structure enveloped by actin filaments, suggesting that the cells undergo differentiation and structural transformation. The expression of vimentin also highlights the confined microenvironment of the scaffold, offering both structural support and functional integration for the cells.[52] The interaction of vimentin protein with phosphorylated extracellular signal-regulated kinase 1 (ERK1) and other signaling proteins (phosphatase-2A and 14−3−3 proteins) specifies the cell-surface receptors and signaling pathway.[53] Large and intensified perinuclear cytoplasmic bundles of vimentin networks formed by the growth of NIH/3T3 and HDFn cells confirm that Z−G micronutrients enhance cellular development and regeneration. It has been reported that Zn, at micromolar concentrations, interacts with the vimentin C328 protein, triggering vimentin reorganization and providing a protective role against oxidative stress in cells.[13] The supplement of Z−G micronutrients showed evidence of the acceleration of vimentin expression. It could be the key factor for the regulation of TGF-β1 and Slug signaling that activates fibroblast for ECM synthesis, and cell−cell contacts to facilitate wound healing.[54] Zinc deficiency impairs vimentin function. The presence of extracellular zinc can interact with vimentin-cystine to form a metalloprotein complex, inducing fluorescence in the intermediate filaments. Notably, the combination of zinc and vimentin is increasingly prevalent in stimulating immune, endothelial, epithelial, and undifferentiated muscle cells for wound repair and cell growth. Therefore, the higher expression of vimentin observed in NIH/3T3 and HDFn cells suggests that PZ2G2 is effective for wound healing and tissue regeneration.

Furthermore, the expression of α-SMA in NIH/3T3 and HDFn cells demonstrates the intrinsic biochemical and robust mechanical properties of the fibrous scaffolds. Notably, α-SMA expression indicates fibroblast contractility, which is crucial for

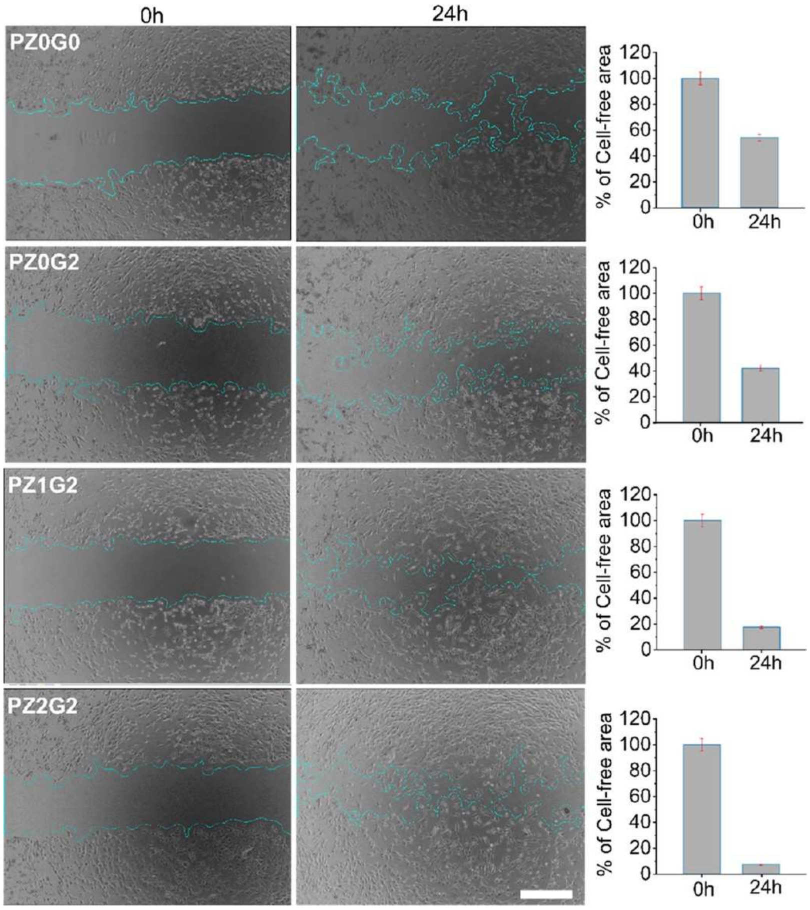

Figure 9. Representative optical images and the corresponding quantitative analysis of the in vitro scratch wound healing assay for HUVECs cultured on extracts of different scaffolds. The migratory ability of HUVECs (left and middle columns) was measured using a wound healing assay tool from the ImageJ software. The images of the cells migrated and spread over the wound area were observed and photographed using a phase contrast inverted microscope at 0 and 24 h. Scale bar = 500 μm. Corresponding bar graphs in the right column represent the quantitative analysis illustrating the percentage of cell-free area at a given time interval during the scratch wound assay.

the wound healing process.[55] During the time-course evaluation of the immunofluorescence images, the α-SMA expression was also higher on day 14 than on day 6 (Figure S8A). A trend in protein expression was observed with PZ0G0 < PZ0G2 < PZ1G2 < PZ2G2 at day 14, indicating that the cells were highly proliferated and either activated or modulated into myofibroblasts. It has been suggested that the expression of α-SMA reflects the phenotypic transition of fibroblasts to myofibroblasts, which contributes to the increased contractile force generated by the cells.[56] Importantly, myofibroblasts secrete fibronectin (FN) and collagen, which provide them with a contractile ability and contribute to the regeneration of granulation tissue. This process protects the wound surface from microbial invasion, helps suppress the escalation of injury, and facilitates the remodeling of the wound with new tissue and vasculature.[15] The strong expression of α-SMA crossing the cell cytoplasm within vimentin indicates cell differentiation, transformation, and phase changes in both cell types to stimulated myofibroblasts. Zn hemostasis in ECM stimulates the fibroblasts in wound healing ability through upregulation of cell cycle proteins, p38-MAPK (mitogen-activated protein kinase), and ERK1/2 signaling pathways, reaching their maximum proliferation rate in 2−4 days.[57] The expression of α-SMA is inhibited significantly in the presence of Zn more than 100 μM along the TGF-β singling pathway.[58] However, the presence of zein in the Z−G combination controlled the degradation and aggregation of zinc, reducing its concentration to avoid an overdose. Thus, the synergistic effect of the natural protein and micronutrients in the PZ2G2 scaffolds enhanced protein expression in NIH/3T3 fibroblasts and HDFn, reflecting cellular hypertrophy and hyperplasia. This suggests long-term implications for wound repair and tissue regeneration. Moreover, we quantified the expression of DAPI, vimentin, and α-SMA proteins corresponding to immunofluorescence images as shown in Figure 8((B,C for NIH/3T3) and (E,F for HDFn)). The immunofluorescence intensity of DAPI was found to be relatively consistent on the scaffold samples, indicating the more viable cells. The evaluation of in vitro cellular activities reveals that there was no reduced cellular mass, cell density, and apoptosis at increased cultured time, insisting that the cells grown on the scaffolds were without notable toxicity. Further, the intensity of α-SMA expressed by cells on PZ0G0 and PZ0G2 at day 6 (Figure 8B) showed higher levels than with PZ1G2 and PZ2G2 scaffolds but no significant difference was observed. This indicates the cells might be in transition phases on day 6. Notably, both fluorescent microscopy images and immunofluorescence images confirm the widespread extension of cell mass and well-expressed cytoplasmic proteins on Z−G-based scaffolds. As expected, the intensity of α-SMA on PZ2G2 scaffolds significantly increased on day 14 compared to PZ1G2 scaffolds ($p < 0.05$) in NIH/3T3 and ($p < 0.001$) in HDFn. In addition,

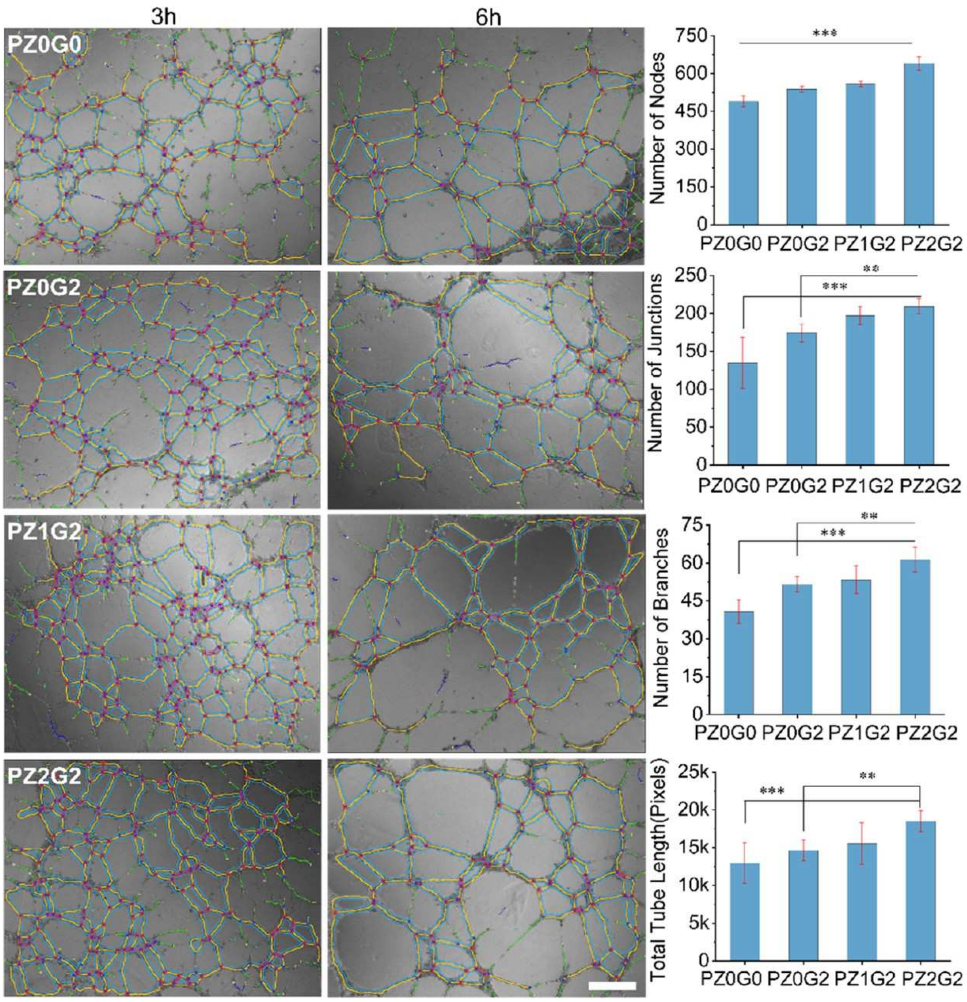

Figure 10. In vitro angiogenic potential of the fibrous scaffolds and effects on tube formation. The formation of a capillary-like network by HUVECs, in response to stimulation from the extracted media, was observed and photographed using an inverted microscope at 3 and 6 h. Scale bar = 500 μm. Right bar graphs: Respective images of 6 h were used to perform analysis of tube formation by using the Angiogenesis plugin from ImageJ software. Different parameters were reported to measure tube forming ability, number of nodes, junctions, meshes, and tube length ($n = 3$, in triplicate). Statistical analysis was performed using the one-way ANOVA with Tukey's post hoc method, and the data are expressed as the mean ± SD; $n = 3$ per group (where $^{**}p < 0.01$ and $^{***}p < 0.001$).

NIH/3T3 cells and HDFn on PZ2G2 scaffolds had an all-time higher intensity of vimentin expression than all other scaffolds. The higher wt % of Z−G particles in PZ2G2 significantly enhanced ($p < 0.05$) the vimentin expression compared to PZ1G2 suggesting that the PZ2G2 scaffolds maintain the threshold concentration of Zn micronutrients. In addition, the expression of vimentin promotes cell motility, maintaining cell shape and integrity of the cytoplasm in the cytoskeleton.[59] Increased vimentin expression indicates an epithelial-mesenchymal transition and fibroblast activation, influencing mechanical adaptation and stiffness. The high levels of α-SMA and vimentin on the PZ2G2 scaffolds likely result from enhanced interactions with Z−G micronutrients. Extracellular zinc ions or Z−G complexes may regulate ECM interactions and protein expression, suggesting a role in fibroblast phenotype regulation and myofibroblast differentiation.[60]

4.9. In Vitro Angiogenic Potential of HUVECs.

4.9.1. Cell Migration. We performed an in vitro wound healing assay to assess the closure of an artificially induced wound on a cellular monolayer on a cell culture plate. The optical images in Figure 9 illustrate the scratch wound healing process. The migration of HUVECs cultured with extracts from the different scaffolds was enhanced compared to that of the control media (figure not included). HUVECs cultured with the extracts demonstrated significantly denser cell proliferation and migrated more effectively toward the scratched area. The Zn ions have been known to modulate cellular signal recognition that activates cells for spreading, proliferation, and migration.[61] The migration rates of HUVEC increased significantly with the extracts from zinc-based scaffolds compared with those without Zn. The corresponding bar graphs of Figure 9 show that after 24 h of incubation of cells with the extract of different scaffolds, the cell-free area was found to be 54.04, 41.96, 17.50, and 7.37%, respectively. Almost 93 and 82% of the wound area were occupied by migrated cells in the PZ2G2 and PZ1G2, respectively. While the samples without Zn covered about 52%, which means almost 33% less than the Zn-based scaffolds. These results indicate that the recovery rate of HUVECs cultured on PZ2G2 extracts significantly improved and promoted wound healing.

4.9.2. Tube Formation/Neovascularization. Angiogenesis is a crucial part of wound healing, involving the formation of new blood vessels to supply nutrients and regulate fibroblast activity. This process, along with fibroblast survival, prolifer-

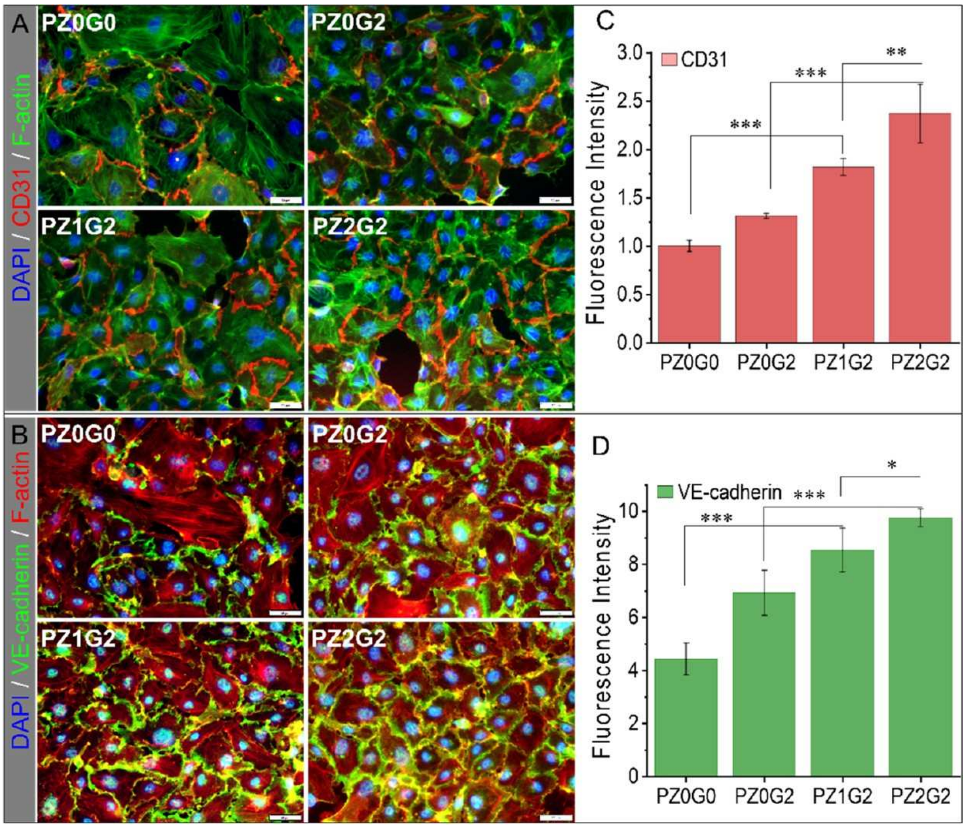

Figure 11. In vitro angiogenic potential of the fibrous scaffolds and their effects on the formation of vasculature. Immunofluorescence images displaying the endothelial-junction-associated protein markers, CD31 (red) (A), and VE-cadherin (green) (B) by the HUVECs cultured under-extracted medium from different nanofibrous scaffolds for seven days. F-actin in (A, B) was labeled with ActinGreen 488 ReadyProbes Reagents (Alexa Fluor 488 phalloidin) and ActinRed 555 ReadyProbes Reagents (Rhodamine phalloidin), respectively. Scale bar = 50 μm. (C, D) Quantification of the expression of CD31 and VE-cadherin of respective immunofluorescence images. The intensities were measured from the expression of the proteins in immunofluorescence images by the ImageJ software. Statistical analysis was performed using the one-way ANOVA with Tukey's post hoc method, and the data are expressed as the mean ± SD; $n = 3$ per group (where $^*p < 0.05$, $^{**}p < 0.01$, and $^{***}p < 0.001$).

ation, and differentiation, supports the formation of new connective tissue and aids in overall wound healing and tissue remodeling.[62] To evaluate the angiogenic activity on different fibrous scaffolds, HUVEC cell migration and vascular tube formation experiments were conducted. Endothelial cell migration is a crucial step in blood vessel development and vascular remodeling. These findings support the idea that Zn-stimulated wound healing is associated with angiogenic activation in defect areas. Endothelial tubular network formation involves key angiogenesis processes such as cell proliferation and migration, and these cells align when seeded on a basement membrane matrigel matrix.[63] The endothelial cells spontaneously differentiate and reorganize to form tubular structures, forming junctions, mesh-like networks, nodes, and branches across the matrix. The tube formation assay provides an additional qualitative and quantitative evaluation of cell behavior. After seeding HUVECs onto the Matrigel matrix with extract of different scaffolds, the cells self-assembled and elongated, and tube-like aggregation was observed as early as 3 h (Figure 10). The optical images (left column) show a profound vessel-like networking formation and branch numbers at early time points (3–6 h). To quantitatively evaluate angiogenesis, crucial parameters of tubular networking—such as the number of nodes, junctions, meshes, and tube length—were measured using the Angiogenesis Plugin for ImageJ software (right column). The Zn-containing scaffolds enhanced the HUVECs to display the greatest ability with significant value ($p < 0.01$ and $p < 0.001$) to form the tube length (from 15,542.67 ± 2758.26 to 18,466.33 ± 1403.19, pixels), node numbers (from 558 ± 11.532 to 639 ± 27.184), junctions (from 197 ± 12.124 to 209 ± 10.149), and branch numbers (from 53.33 ± 5.507 to 61.333 ± 4.933) compared to these on PZ0G0 and PZ0G2. The arrangement of cell–cell junctions and tube alignment indicates endothelial differentiation in new blood vessel formation. The robust network formation requires cell mobility, so the enhanced migration capabilities observed with Zn ions may contribute to the organization of cells into tube structures. A smaller cluster of cells rather than the tube extensions is seen in PZ0G0 and PZ0G2 aa compared to the PZ1G2 and PZ2G2 samples, which may be due to the lack of mobility noted with cell migration. The tubes persisted longer in the Zn composite sample groups. The results indicate that extracts from the fibrous scaffold containing Zn ions significantly stimulate endothelial functions in vitro, such as cellular migration and tubular network formation. The migrated endothelial cells form capillary-like networks and mature into vascular systems, as observed in prior publications.[64]

4.9.3. Vascular Differentiation of HUVECs. The promotion of angiogenesis and formation of vasculature morphology of HUVECs were assessed through immunocytochemistry (Figure 11). To observe morphological changes and blood-vessel-like organization, CD31 and VE-cadherin, key markers for vascular differentiation, were used. These markers are essential for evaluating neovascularization. CD31 is crucial for elongation, migration, and cell−cell association in forming network structures, while VE-cadherin is important for cell−cell association and also contributes to vacuole fusion and intercellular lumen formation.[65] The immunofluorescence images (Figure 11A) showed the expression of the vascular endothelial tight junction molecule, CD31. As shown in Figure 11A, HUVECs cultured with the extracts of different composite scaffolds proliferated and formed a monolayer with increased tight junctions at day 7. A significant increase in the density and degree of neovascularization with PZ2G2 extract media is seen compared to other sample groups. The majority of the cells expressed CD31 protein markers, with a red circle around the entire periphery of the nuclei interconnected between the cells indicating the vascular differentiation of HUVECs. More neovascular and larger vessel diameters were found in the PZ1G2 and PZ2G2 groups. The quantitative analysis of the respective fluorescence images (Figure 11C) shows that the Zn induced the highest expression level of the bold vessel phenotype markers, CD31, which is significantly higher ($p < 0.001$) than other sample groups. In addition, the level of expression of CD31 steadily increased with cell proliferation, and many tight junction proteins were observed throughout the cell membrane.

Furthermore, vascular endothelial cell-to-cell adherent junctions were visualized through the immunofluorescence staining of VE-cadherin, which is crucial for maintaining vascular permeability and integrity.[66] The proliferation and attachment of cells depend upon cell−cell linkages, such as tight junctions and cadherins. In Figure 11B, the expression of VE-cadherin was significantly higher and distributed across the cell membrane, highlighting the formation of cohesive and organized intercellular junctions with the PZ1G2 and PZ2G2 scaffolds. In the PZ0G0 and PZ0G2 scaffolds, VE-cadherin expression was weak, intermittent, and punctated along the cell−cell borders of endothelial cells. In contrast, VE-cadherin staining and expression were intense and continuously distributed around the entire periphery of cells in the PZ2G2 extract. The result of fewer expression and altered distribution of VE-cadherin suggests that the endothelial barrier is disrupted and vascular permeability is increased.[67] The immunofluorescence intensity data (Figure 11D) show that the VE-cadherin expression was significantly higher in the Zn-containing sample groups. These results indicate that extracts from the PZ1G2 and PZ2G2 scaffolds effectively induced HUVECs to form tubes and undergo neovascularization. The Zn ions from the PZ1G2 and PZ2G2 scaffolds enhanced cell proliferation, as indicated by greater and stronger expression of VE-cadherin. This reflects cellular hypertrophy and hyperplasia, suggesting potential long-term benefits for wound repair and tissue regeneration.

5. CONCLUSIONS

In summary, we report the fabrication of zein-coated zinc-particle-embedded fibrous scaffolds with enhanced physical and biochemical functionalities, providing invaluable cues for fibroblast regeneration and differentiation. Our approach establishes a simple and easily accessible surface coating strategy, enabling the binding affinity of zinc to zein protein and ensuring the bioavailability of zinc nanoparticles as Z−G micronutrients. The biological performance of zinc nanoparticles was enhanced through linkage with the zein protein. This protein supports zinc homeostasis through controlled release, closely mimicking ECM deposition that is suitable for cell-scaffold interactions. A variety of scaffolds with nanofiber structures at different ratios of Z−G particles were exemplified via physicochemical and biological properties. The fibrous scaffolds incorporated with Z−G particles at 2.4 wt % significantly enhanced structural integrity, robust mechanical strength, and hydrophilicity. Importantly, through the use of NIH/3T3 cells and HDFn, in vitro cell-laden scaffolds demonstrated improved cell viability, proliferation, and differentiation. The expression of cytoskeleton proteins including vimentins and α-SMA confirmed the differentiation of NIH/3T3 cells and HDFn toward myofibroblasts. Additionally, our in vitro wound healing assay, migration and tube formation experiments, and immunocytochemistry evaluation demonstrated that the engineered scaffolds effectively encouraged HUVECs to exhibit angiogenic activity, including the formation of new blood. vessels and neovascularization. These results suggest that protein-coated zinc nanoparticles can enhance cell-to-cell interaction and communication while maintaining protein-rich micronutrients as a supplement to the extracellular matrix (ECM) for cell growth and activity. We believe that this self-enhanced micronutrient scaffold can provide a cellular microenvironment that promotes wound repair and tissue regeneration.

■ ASSOCIATED CONTENT

Supporting Information

The Supporting Information is available free of charge at https://pubs.acs.org/doi/10.1021/acsami.4c13458.

> Characterization of zein and zein-coated Zn particles using FTIR and XPS analysis; in vitro cell viability study; fluorescence microscopy images of fibroblasts showing the effect of scaffold on cell attachment and morphology; immunocytochemistry images of fibroblasts showing the heterogeneity of fibroblasts; and immunofluorescence images displaying the endothelial junctions (PDF)

■ AUTHOR INFORMATION

Corresponding Author

Narayan Bhattarai − *Department of Chemical, Biological and Bioengineering, North Carolina A&T State University, Greensboro, North Carolina 27411, United States;* orcid.org/0000-0002-0583-7913; Email: nbhattar@ncat.edu

Authors

Sita Shrestha − *Department of Chemical, Biological and Bioengineering, North Carolina A&T State University, Greensboro, North Carolina 27411, United States*

Bishnu Kumar Shrestha − *Department of Chemical, Biological and Bioengineering, North Carolina A&T State University, Greensboro, North Carolina 27411, United States; Department of Chemistry, North Carolina A&T State University, Greensboro, North Carolina 27411, United States*

Felix Tettey-Engmann − *Department of Chemical, Biological and Bioengineering, North Carolina A&T State University, Greensboro, North Carolina 27411, United States; Department of Industrial and Systems Engineering, North Carolina A&T State University, Greensboro, North Carolina 27411, United States*

Reedwan Bin Zafar Auniq − *Department of Nanoengineering, Joint School of Nanoscience and Nanoengineering (JSNN), North Carolina A&T State University, Greensboro, North Carolina 27401, United States*

Kiran Subedi − *Analytical Services Laboratory, College of Agriculture and Environmental Sciences, North Carolina A&T State University, Greensboro, North Carolina 27411, United States*

Sanjaya Ghimire − *Department of Chemical, Biological and Bioengineering, North Carolina A&T State University, Greensboro, North Carolina 27411, United States*

Salil Desai − *Department of Industrial and Systems Engineering, North Carolina A&T State University, Greensboro, North Carolina 27411, United States;* orcid.org/0000-0002-6116-2105

Complete contact information is available at:
https://pubs.acs.org/10.1021/acsami.4c13458

Notes

The authors declare no competing financial interest.

■ ACKNOWLEDGMENTS

This work was supported financially by the National Science Foundation-Excellence in Research (NSF-EiR 2100861). Part of this research work was also supported by NSF-Engineering Research Centers (NSF-ERC, 2133630) and Center of Excellence in Product Design and Advanced Manufacturing (CEPDAM). The authors thank Dr. Bishnu P. Bastakoti, Dr. Gayani Pathiraja, Mr. Binod K.C., and Jonathan Appiah for their technical assistance in research. They also acknowledge Dr. Waterman's lab for donating them human dermal fibroblast cells. Characterization of the scaffolds was also performed in part at the Joint School of Nanoscience and Nanoengineering (SENIC-NNCI), which is supported by the National Science Foundation (NSF ECCS-1542174) and facilities of College of Engineering. The authors acknowledge the Analytical Services Laboratory at the College of Agriculture and Environmental Sciences, North Carolina A&T State University, for their valuable support in facilitating the sample preparation and elemental analysis.

■ REFERENCES

(1) Broughton, G.; Janis, J. E.; Attinger, C. E. The basic science of wound healing. *Plast. Reconstr. Surg.* **2006**, *117*, 12S−34S.

(2) Holmes, A. D. Wound Healing. *N. Engl. J. Med.* **1942**, *227*, 909−921.

(3) Sani, E. S.; Xu, C.; Wang, C.; Song, Y.; Min, J.; Tu, J.; Solomon, S. A.; Li, J.; Banks, J. L.; Armstrong, D. G.; Gao, W. A stretchable wireless wearable bioelectronic system for multiplexed monitoring and combination treatment of infected chronic wounds. *Sci. Adv.* **2023**, *9*, No. eadf7388.

(4) Cho, N. H.; Guerrero-Martínez, A.; Ma, J.; Bals, S.; Kotov, N. A.; Liz-Marzán, L. M.; Nam, K. T. Bioinspired chiral inorganic nanomaterials. *Nat. Rev. Bioeng.* **2023**, *1*, 88−106.

(5) Kornblatt, A. P.; Nicoletti, V. G.; Travaglia, A. The neglected role of copper ions in wound healing. *J. Inorg. Biochem.* **2016**, *161*, 1−8.

(6) Chen, B.; Yu, P.; Chan, W. N.; Xie, F.; Zhang, Y.; Liang, L.; Leung, K. T.; Lo, K. W.; Yu, J.; Tse, G. M.; et al. Cellular zinc metabolism and zinc signaling: from biological functions to diseases and therapeutic targets. *Signal Transduction Targeted Ther.* **2024**, *9*, No. 6.

(7) Mostaed, E.; Sikora-Jasinska, M.; Drelich, J. W.; Vedani, M. Zinc-based alloys for degradable vascular stent applications. *Acta Biomater.* **2018**, *71*, 1−23.

(8) Sreenivasamurthy, S. A.; Akhter, F. F.; Akhter, A.; Su, Y.; Zhu, D. Cellular mechanisms of biodegradable zinc and magnesium materials on promoting angiogenesis. *Biomater. Adv.* **2022**, *139*, No. 213023.

(9) Taylor, G. A.; Blackshear, P. J. Zinc inhibits turnover of labile mRNAs in intact cells. *J. Cell. Physiol.* **1995**, *162*, 378−387.

(10) Wiggins, R. C.; Bouma, B. N.; Cochrane, C. G.; Griffin, J. H. Role of high-molecular-weight kininogen in surface-binding and activation of coagulation Factor XI and prekallikrein. *Proc. Natl. Acad. Sci. U.S.A.* **1977**, *74*, 4636−4640.

(11) Yang, F.; Xue, Y.; Wang, F.; Guo, D.; He, Y.; Zhao, X.; Yan, F.; Xu, Y.; Xia, D.; Liu, Y. Sustained release of magnesium and zinc ions synergistically accelerates wound healing. *Bioact. Mater.* **2023**, *26*, 88−101.

(12) Irie, M.; Kabata, H.; Sasahara, K.; Kurihara, M.; Shirasaki, Y.; Kamatani, T.; Baba, R.; Matsusaka, M.; Koga, S.; Masaki, K.; et al. Annexin A1 is a cell-intrinsic metalloregulator of zinc in human ILC2s. *Cell Rep.* **2023**, *42*, No. 112610.

(13) Pérez-Sala, D.; Oeste, C. L.; Martínez, A. E.; Carrasco, M. J.; Garzón, B.; Canada, F. J. Vimentin filament organization and stress sensing depend on its single cysteine residue and zinc binding. *Nat. Commun.* **2015**, *6*, No. 7287.

(14) Tettey, F.; Saudi, S.; Davies, D.; Shrestha, S.; Johnson, K.; Fialkova, S.; Subedi, K.; Bastakoti, B. P.; Sankar, J.; Desai, S.; Bhattarai, N. Fabrication and characterization of Zn particle incorporated fibrous scaffolds for potential application in tissue healing and regeneration. *ACS Appl. Mater. Interfaces* **2023**, *15*, 48913−48929.

(15) Botella, H.; Peyron, P.; Levillain, F.; Poincloux, R.; Poquet, Y.; Brandli, I.; Wang, C.; Tailleux, L.; Tilleul, S.; Charrière, G. M.; et al. Mycobacterial P1-type ATPases mediate resistance to zinc poisoning in human macrophages. *Cell Host Microbe* **2011**, *10*, 248−259.

(16) Rahman, M.; Dip, T. M.; Haase, T.; Truong, Y. B.; Le, T. C.; Houshyar, S. Fabrication of Zein-Based Fibrous Scaffolds for Biomedical Applications—A Review. *Macromol. Mater. Eng.* **2023**, *308*, No. 2300175.

(17) Burrows, C. J.; Harper, J. B.; Sander, W.; Tantillo, D. J. Solvation effects in organic chemistry. *J. Org. Chem.* **2022**, *87*, 1599−1601.

(18) Satpathy, A.; Pal, A.; Sengupta, S.; Das, A.; Hasan, M. M.; Ratha, I.; Barui, A.; Bodhak, S. Bioactive nano-hydroxyapatite doped electrospun PVA-chitosan composite nanofibers for bone tissue engineering applications. *J. Indian Inst. Sci.* **2019**, *99*, 289−302.

(19) Wang, H.; Wang, P.; Li, B.; Mao, H. Study on the Growth and Mechanism of Zinc Nanostructures on an Ionic Liquid Substrate. *Cryst. Growth Des.* **2020**, *20*, 892−899.

(20) Huang, L.; Wang, J.; Watkins, A. M.; Das, R.; Lilley, D. M. J. Structure and ligand binding of the glutamine-II riboswitch. *Nucleic Acids Res.* **2019**, *47*, 7666−7675.

(21) Mayerhöfer, T. G.; Pahlow, S.; Hubner, U.; Popp, J. Removing interference-based effects from the infrared transflectance spectra of thin films on metallic substrates: a fast and wave optics conform solution. *Analyst* **2018**, *143*, 3164−3175.

(22) Zou, X.-X.; Li, G.; Zhao, J.; Wang, P.; Wang, Y.; Zhou, L.; Su, J.; Li, L.; Chen, J. Light-driven transformation of ZnS-cyclohexylamine nanocomposite into zinc hydroxysulfate: a photochemical route to inorganic nanosheets. *Inorg. Chem.* **2011**, *50*, 9106−9113.

(23) Wang, L.; Huang, X.; Cao, X.; Zhou, F.; Liu, B.; Wei, S.; Liu, X.; Yang, X.; Yin, S. Confining the Growth of AgNPs onto Epigallocatechin Gallate-Decorated Zein Nanoparticles for Constructing Potent Protein-Based Antibacterial Nanocomposites. *J. Agric. Food Chem.* **2024**, *72*, 4928−4938.

(24) Shrestha, S.; Shrestha, B. K.; Lee, J.; Joong, O. K.; Kim, B.; Park, C. H.; Kim, C. S. A conducting neural interface of polyurethane/silk-functionalized multiwall carbon nanotubes with enhanced mechanical strength for neuroregeneration. *Mater. Sci. Eng.: C* **2019**, *102*, 511−523.

(25) Shrestha, S.; Shrestha, B. K.; Ko, S. W.; Kandel, R.; Park, C. H.; Kim, C. S. Engineered cellular microenvironments from functionalized multiwalled carbon nanotubes integrating Zein/Chitosan@Polyurethane for bone cell regeneration. *Carbohydr. Polym.* **2021**, *251*, No. 117035.

(26) Maret, W.; Li, Y. Coordination dynamics of zinc in proteins. *Chem. Rev.* **2009**, *109*, 4682−4707.

(27) Biswal, B. K.; El Sadany, M.; Kumari, D.; Sagar, P.; Singhal, N. K.; Sharma, S.; Stobdan, T.; Shanmugam, V. Twin function of zein−zinc coordination complex: wheat nutrient enrichment and nanoshield against pathogenic infection. *ACS Sustainable Chem. Eng.* **2018**, *6*, 5877−5887.

(28) Wan, Y.; Lu, X.; Dalai, S.; Zhang, J. Thermophysical properties of polycaprolactone/chitosan blend membranes. *Thermochim. Acta* **2009**, *487*, 33−38.

(29) Cooper-White, J.; Mackay, M. E. Rheological properties of poly(lactides). Effect of molecular weight and temperature on the viscoelasticity of poly(l-lactic acid). *J. Polym. Sci., Part B: Polym. Phys.* **1999**, *37*, 1803−1814.

(30) Nayar, D. Small crowder interactions can drive hydrophobic polymer collapse as well as unfolding. *Phys. Chem. Chem. Phys.* **2020**, *22*, 18091−18101.

(31) Cheng, X.; Li, T.; Yan, L.; Jiao, Y.; Zhang, Y.; Wang, K.; Cheng, Z.; Ma, J.; Shao, L. Biodegradable electrospinning superhydrophilic nanofiber membranes for ultrafast oil-water separation. *Sci. Adv.* **2023**, *9*, No. eadh8195.

(32) Lampin, M.; Warocquier-Clérout, R.; Legris, C.; Degrange, M.; Sigot-Luizard, M. F. Correlation between substratum roughness and wettability, cell adhesion, and cell migration. *J. Biomed. Mater. Res.* **1997**, *36*, 99−108.

(33) Metze, F. K.; Sant, S.; Meng, Z.; Klok, H.; Kaur, K. Swelling-Activated, Soft Mechanochemistry in Polymer Materials. *Langmuir* **2023**, *39*, 3546−3557.

(34) Niedzwiecki, D. J.; Grazul, J.; Movileanu, L. Single-molecule observation of protein adsorption onto an inorganic surface. *J. Am. Chem. Soc.* **2010**, *132*, 10816−10822.

(35) Li, J.; Celiz, A. D.; Yang, J.; Yang, Q.; Wamala, I.; Whyte, W.; Seo, B. R.; Vasilyev, N. V.; Vlassak, J. J.; Suo, Z.; Mooney, D. J. Tough adhesives for diverse wet surfaces. *Science* **2017**, *357*, 378−381.

(36) Plath, A.; Facchi, S. P.; Souza, P. R.; Sabino, R. M.; Corradini, E.; Muniz, E. C.; Popat, K. C.; Filho, L.; Kipper, M. J.; Martins, A. F. Zein supports scaffolding capacity toward mammalian cells and bactericidal and antiadhesive properties on poly (ε-caprolactone)/zein electrospun fibers. *Mater. Today Chem.* **2021**, *20*, No. 100465.

(37) Chen, D.; Oezguen, N.; Urvil, P.; Ferguson, C.; Dann, S. M.; Savidge, T. C. Regulation of protein-ligand binding affinity by hydrogen bond pairing. *Sci. Adv.* **2016**, *2*, No. e1501240.

(38) Pirro, F.; La Gatta, S.; Arrigoni, F.; Famulari, A.; Maglio, O.; Del Vecchio, P.; Chiesa, M.; De Gioia, L.; Bertini, L.; Chino, M.; et al. A De novo-designed type 3 copper protein tunes catechol substrate recognition and reactivity. *Angew. Chem., Int. Ed.* **2023**, *62*, No. e202211552.

(39) Li, M.; Ogiso, M.; Minoura, N. Enzymatic degradation behavior of porous silk fibroin sheets. *Biomaterials* **2003**, *24*, 357−365.

(40) Tuli, H. S.; Joshi, R.; Kaur, G.; Garg, V. K.; Sak, K.; Varol, M.; Kaur, J.; Alharbi, S. A.; Alahmadi, T. A.; Aggarwal, D.; et al. Metal nanoparticles in cancer: from synthesis and metabolism to cellular interactions. *J. Nanostruct. Chem.* **2023**, *13*, 321−348.

(41) Weiss, A.; Murdoch, C. C.; Edmonds, K. A.; Jordan, M. R.; Monteith, A. J.; Perera, Y. R.; Nassif, A. M. R.; Petoletti, A. M.; Beavers, W. N.; Munneke, M. J.; et al. Zn-regulated GTPase metalloprotein activator 1 modulates vertebrate zinc homeostasis. *Cell* **2022**, *185*, 2148−2163.e27.

(42) Horton, T. M.; Allegretti, P. A.; Lee, S.; Moeller, H. P.; Smith, M.; Annes, J. P. Zinc-chelating small molecules preferentially accumulate and function within pancreatic β cells. *Cell Chem. Biol.* **2019**, *26*, 213−222.e6.

(43) Zalewski, P. D.; Millard, S. H.; Forbes, I. J.; Kapaniris, O.; Slavotinek, A.; Betts, W. H.; Ward, A. D.; Lincoln, S. F.; Mahadevan, I. Video image analysis of labile zinc in viable pancreatic islet cells using a specific fluorescent probe for zinc. *J. Histochem. Cytochem.* **1994**, *42*, 877−884.

(44) Oteiza, P. I. Zinc and the modulation of redox homeostasis. *Free Radical Biol. Med.* **2012**, *53*, 1748−1759.

(45) Li, C.; Sun, F.; Tian, J.; Li, J.; Sun, H.; Zhang, Y.; Guo, S.; Lin, Y.; Sun, X.; Zhao, Y. Continuously released Zn2+ in 3D-printed PLGA/β-TCP/Zn scaffolds for bone defect repair by improving osteoinductive and anti-inflammatory properties. *Bioact. Mater.* **2023**, *24*, 361−375.

(46) Soenen, S. J.; Parak, W. J.; Rejman, J.; Manshian, B. (Intra)Cellular Stability of Inorganic Nanoparticles: Effects on Cytotoxicity, Particle Functionality, and Biomedical Applications. *Chem. Rev.* **2015**, *115*, 2109−2135.

(47) Liu, Z.; Tang, W.; Liu, J.; Han, Y.; Yan, Q.; Dong, Y.; Liu, X.; Yang, D.; Ma, G.; Cao, H. A novel sprayable thermosensitive hydrogel coupled with zinc modified metformin promotes the healing of skin wound. *Bioact. Mater.* **2023**, *20*, 610−626.

(48) Yang, K.; Lee, M.; Jones, P. A.; Liu, S. S.; Zhou, A.; Xu, J.; Sreekanth, V.; Wu, J. L. Y.; Vo, L.; Lee, E. A.; Pop, R.; Lee, Y.; Wagner, B. K.; Melton, D. A.; Choudhary, A.; Karp, J. M. A 3D culture platform enables development of zinc-binding prodrugs for targeted proliferation of β cells. *Sci. Adv.* **2020**, *6*, No. eabc3207.

(49) Egefjord, L.; Petersen, A. B.; Bak, A.; Rungby, J. Zinc, alpha cells and glucagon secretion. *Curr. Diabetes Rev.* **2010**, *6*, 52−57.

(50) Wen, Z.; Shi, X.; Li, X.; Liu, W.; Liu, Y.; Zhang, R.; Yu, Y.; Su, J. Mesoporous TiO2 Coatings Regulate ZnO Nanoparticle Loading and Zn2+ Release on Titanium Dental Implants for Sustained Osteogenic and Antibacterial Activity. *ACS Appl. Mater. Interfaces* **2023**, *15*, 15235−15249.

(51) Jiu, Y.; Lehtimäki, J.; Tojkander, S.; Cheng, F.; Jäälinoja, H.; Liu, X.; Varjosalo, M.; Eriksson, J. E.; Lappalainen, P. Bidirectional Interplay between Vimentin Intermediate Filaments and Contractile Actin Stress Fibers. *Cell. Rep.* **2015**, *11*, 1511−1518.

(52) Kim, H.; Nakamura, F.; Lee, W.; Hong, C.; Pérez-Sala, D.; McCulloch, C. A. Regulation of cell adhesion to collagen via beta1 integrins is dependent on interactions of filamin A with vimentin and protein kinase C epsilon. *Exp. Cell Res.* **2010**, *316*, 1829−1844.

(53) Chang, L.; Goldman, R. D. Intermediate filaments mediate cytoskeletal crosstalk. *Nat. Rev. Mol. Cell Biol.* **2004**, *5*, 601−613.

(54) Cheng, F.; Eriksson, J. E. Intermediate Filaments and the Regulation of Cell Motility during Regeneration and Wound Healing. *Cold Spring Harbor Perspect. Biol.* **2017**, *9*, No. a022046.

(55) Hinz, B.; Celetta, G.; Tomasek, J. J.; Gabbiani, G.; Chaponnier, C. Alpha-smooth muscle actin expression upregulates fibroblast contractile activity. *Mol. Biol. Cell* **2001**, *12*, 2730−2741.

(56) Xu, H.; Bai, D.; Ruest, L.; Feng, J. Q.; Guo, Y.; Tian, Y.; Jing, Y.; He, Y.; Han, X. Expression analysis of α-smooth muscle actin and tenascin-C in the periodontal ligament under orthodontic loading or in vitro culture. *Int. J. Oral Sci.* **2015**, *7*, 232−241.

(57) Chen, C.; Du, J.; Feng, W.; Song, Y.; Lu, Z.; Xu, M.; Li, Z.; Zhang, Y. β-Adrenergic receptors stimulate interleukin-6 production through Epac-dependent activation of PKCδ/p38 MAPK signalling in neonatal mouse cardiac fibroblasts. *Br. J. Pharmacol.* **2012**, *166*, 676−688.

(58) Kang, M.; Zhao, L.; Ren, M.; Deng, M.; Li, C. Zinc mediated hepatic stellate cell collagen synthesis reduction through TGF-β signaling pathway inhibition. *Int. J. Clin. Exp. Med.* **2015**, *8*, 20463−20471.

(59) Xu, K.; Wang, Z.; Copland, J. A.; Chakrabarti, R.; Florczyk, S. J. 3D porous chitosan-chondroitin sulfate scaffolds promote epithelial to mesenchymal transition in prostate cancer cells. *Biomaterials* **2020**, *254*, No. 120126.

(60) Costigliola, N.; Ding, L.; Burckhardt, C. J.; Han, S. J.; Gutierrez, E.; Mota, A.; Groisman, A.; Mitchison, T. J.; Danuser, G. Vimentin fibers orient traction stress. *Proc. Natl. Acad. Sci. U.S.A.* **2017**, *114*, 5195−5200.

(61) Ma, J.; Zhao, N.; Zhu, D. Endothelial cellular responses to biodegradable metal zinc. *ACS Biomater. Sci. Eng.* **2015**, *1*, 1174−1182.

(62) Demidova-Rice, T. N.; Durham, J. T.; Herman, I. M. Wound healing angiogenesis: innovations and challenges in acute and chronic wound healing. *Adv. Wound Care* **2012**, *1*, 17−22.

(63) Arnaoutova, I.; George, J.; Kleinman, H. K.; Benton, G. The endothelial cell tube formation assay on basement membrane turns 20: state of the science and the art. *Angiogenesis* **2009**, *12*, 267−274.

(64) Franco, C. A.; Jones, M. L.; Bernabeu, M. O.; Geudens, I.; Mathivet, T.; Rosa, A.; Lopes, F. M.; Lima, A. P.; Ragab, A.; Collins, R. T. Dynamic endothelial cell rearrangements drive developmental vessel regression. *PLoS Biol.* **2015**, *13*, No. e1002125.

(65) Davis, G. E.; Camarillo, C. W. An $\alpha 2\beta 1$ integrin-dependent pinocytic mechanism involving intracellular vacuole formation and coalescence regulates capillary lumen and tube formation in three-dimensional collagen matrix. *Exp. Cell Res.* **1996**, *224*, 39−51.

(66) Giannotta, M.; Trani, M.; Dejana, E. VE-cadherin and endothelial adherens junctions: active guardians of vascular integrity. *Dev. Cell* **2013**, *26*, 441−454.

(67) Yang, B.; Cai, B.; Deng, P.; Wu, X.; Guan, Y.; Zhang, B.; Cai, W.; Schaper, J.; Schaper, W. Nitric oxide increases arterial endotheial permeability through mediating VE-cadherin expression during arteriogenesis. *PLoS One* **2015**, *10*, No. e0127931.